$K^+\Sigma^-$ Photoproduction at the BGO-OD Experiment

Johannes Groß

Masterarbeit in Physik
angefertigt im Physikalischen Institut

vorgelegt der
Mathematisch-Naturwissenschaftlichen Fakultät
der
Rheinischen Friedrich-Wilhelms-Universität
Bonn

September 2019

I hereby declare that this thesis was formulated by myself and that no sources or tools other than those cited were used.

Bonn, ...

Date Signature

1. Gutachter: Prof. Dr. Hartmut Schmieden
2. Gutachter: Prof. Dr. Jochen Dingfelder

Acknowledgements

I would like to thank Prof. Dr. Schmieden for the opportunity to write my Master's thesis in such a rich and interesting scientific field. Furthermore, I would like to thank all members of the BGO-OD group for their open ears, advice and support.

Contents

CHAPTER 1

Introduction

Since its early beginnings, mankind has been puzzled by the question of what holds the universe together at its innermost folds. The ancient Greeks believed that all matter must be consisting of tiny, fundamental, unpartable objects, which they called 'atomos' - a belief that should evolve over the following aeons into much more sophisticated, yet incomplete theories of elementary particles. In 1911, Rutherford impinged α particles on a thin gold foil and measured their deflection, deriving that most of the atom's mass must be concentrated in a small, positively charged center. Building on top of that, Bohr was able to describe how electrons surround the atomic core on orbits and are responsible for spectral lines in 1913. In the following years, scientific progress accelerated: The proton was experimentally proved in 1919, the neutron in 1932. The substructure of these nucleons could be described by Gell-Man and Zweig in 1964 with the quark model, laying the basis of today's state of knowledge - the standard model, describing physical processes as an exchange of gauge bosons between elementary particles, namely quarks and leptons. The standard model was able to celebrate a big success in 2012, as the experimental proof of the Higgs boson was obtained at LHC.

As great as the standard model is able to describe physical processes at a fundamental level, it is incomplete yet, leaving many physical problems unsolved. Figure 1.1 shows the light baryon spectrum in a relativistic quark model with instanton-induced quark forces [1].

The baryons are arranged along the x axis according to their quantum numbers, while the y axis depicts their masses. The blue lines correspond to theoretically predicted resonances, while the colored boxes correspond to experimental findings. The size of the boxes specifies the error range. It can clearly be seen that many more resonances have been theoretically predicted than experimentally observed, especially at higher masses - this is known as the so-called 'missing resonance problem'. In addition to that, problems arise at lower masses: The parity between the two lowest lying N* excitations, namely N(1440)$\frac{1}{2}^+$ and N(1535)$\frac{1}{2}^-$, is reversed. One would naturally expect the lowest state above the ground state to have negative parity. Furthermore, the masses between the two lowest lying negative parity states in the strange and non-strange sector - the $\Lambda(1405)$, which is not shown in figure 1.1, and the N(1535)$\frac{1}{2}^-$ - are reversed, as one would expect the state which contains the s quark to be the heavier one [2].

In order to handle these problems, quark models have been developed in which hadrons are made up of more than three quarks, possibly arranged in a colorless, molecular-like meson-meson or meson-baryon

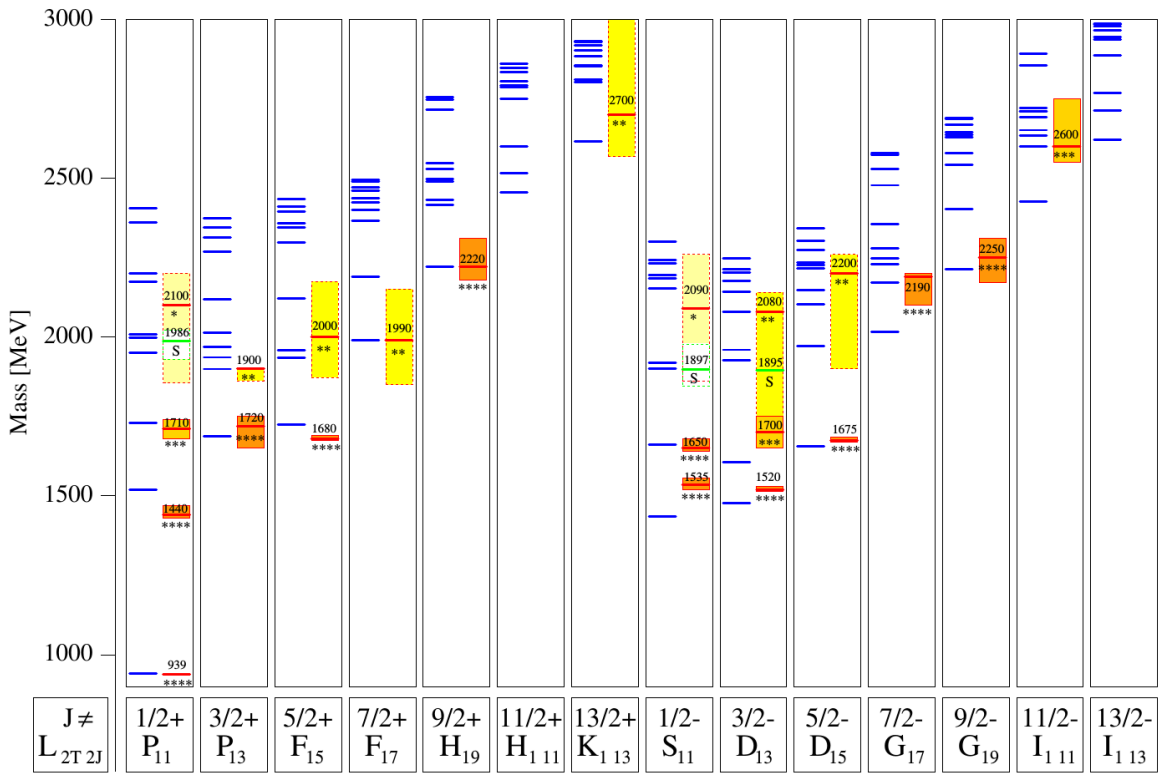

Figure 1.1: Light baryon spectrum (N^* resonances) in a relativistic quark model with instanton-induced quark forces [1]. The x axis describes the baryon quantum numbers, the y axis depicts their masses. Blue lines correspond to theoretically predicted resonances, colored boxes correspond to experimental findings. The size of the boxes specifies the error range

formation[3]. The Goldstone bosons resulting from the symmetry breaking within this model enter as effective 'elementary' objects, enabling interactions of light mesons directly with quarks [4]. A model based on vector meson-baryon interaction was able to predict the recently discovered LHCb pentaquark states in the hidden charm sector [5], also showing good agreement with an experimentally observed pronounced cusp-like structure between $K^*\Lambda$ and $K^*\Sigma$ thresholds in $K^0_S\Sigma^+$ photoproduction off the proton [6]. Thus, the strange sector might be explicable by meson-meson and meson-baryon quark models analogously to the charm sector.

More fundamental research in the strange sector is needed to resolve this issue. Therefore, this Master's thesis focuses on $K^+\Sigma^-$ photoproduction. Yet, only limited data is available for this specific reaction: One data set provided by CLAS as well as one very small data set provided by LEPS are available [7]. This Master's thesis will deliver complementary data, using a novel K^+ identification technique. It is structured as follows:

In chapter 2, the experimental setup of BGO-OD is elucidated, focusing at the tagging system and the central detector, which contains the BGO calorimeter. The forward detector is covered for completeness.

Chapter 3 describes the utilized K^+ identification technique. Most commonly, K^+ are identified in

tracking detectors. However, one can detect K^+ in calorimeters as well by exploiting the fact that the K^+ decays weakly, producing clusters in the calorimeter that are delayed in time. By putting cuts on deposited energy and time, one can distinguish K^+ from other particles.

In chapter 4, the analysis procedure is layed out. For the reaction $\gamma n \rightarrow K^+\Sigma^-$, we had to employ a deuteron target. The deuteron consists of a proton and a neutron, implying the need of getting rid of the background originating from interactions with the proton. This has been done by analysing data from a second target, consisting of protons only. As the photoproductions off the proton and the neutron were incoherent, respectively, we were able to subtract the proton contribution from the data of the deuteron target. This lead up to several corrections, which will all be covered in chapter 4.

Chapter 5 will show the results of the analysis, while chapter 6 will give a summary of this thesis.

CHAPTER 2

The BGO-OD Experiment

The Bismuth Germanate Oxide - Open Dipole (BGO-OD) experiment located at the Electron Stretcher Accelerator (ELSA) at the University of Bonn is a fixed-target experiment especially designed for the investigation of photo-produced forward-going mesons and residual ground as well as excited state baryons with little momentum transfer [2]. It consists of a tagging system, a central detector and a forward spectrometer. The heart of the central detecor is a calorimeter, which is made up of bismuth germanate oxide (BGO), giving the experiment the first part of it's name. The heart of the forward spectrometer is an open dipole magnet (OD), implying the second part of the experiment's name. In this chapter, the diverse technical components of the experimental setup will be elucidated.

2.1 ELSA

ELSA is a three-staged electron accelerator conducted by the Physikalisches Institut (PI), being able to deliver polarized and unpolarized electron beams up to a maximum energy of 3.2 GeV. Amongst others, it is supplying the BGO-OD experiment with a continuous beam current up to several nA. An overview of the accelerator can be seen in figure 2.1.

The first stage of ELSA consists of two linear accelerators (LINACs), whereas LINAC 1 provides an unpolarized electron beam with an energy up to 20 MeV, while LINAC 2 provides a polarized electron beam with a maximum energy of 26 MeV, achieving a maximum polarization of 72.3% ± 0.5%.

The beam is then being fed to the second stage of ELSA, the booster synchrotron. It is able to accelerate electrons to energies ranging from 0.5 GeV to 1.6 GeV at a repetition rate of 50 Hz. The synchrotron operates with a pulsed beam.

Furthermore, the pulsed beam is injected into the third stage of ELSA - the stretcher ring, where it is converted into a continuous beam. The stretcher ring holds a circumference of 270 m and is able to provide the BGO-OD experiment with an electron beam with an energy ranging from 0.5 GeV to 3.2 GeV. The stretcher ring can be operated in stretcher mode, where the electron energy is being kept at the constant level of the booster synchrotron, it can be operated in post-accelerating mode and in storage mode used for synchrotron light experiments. Finally, the beam can be extracted with a current of a few nA and a microscopic duty factor of 100% and led to the experiments, such as BGO-OD and Crystal Barrel [9].

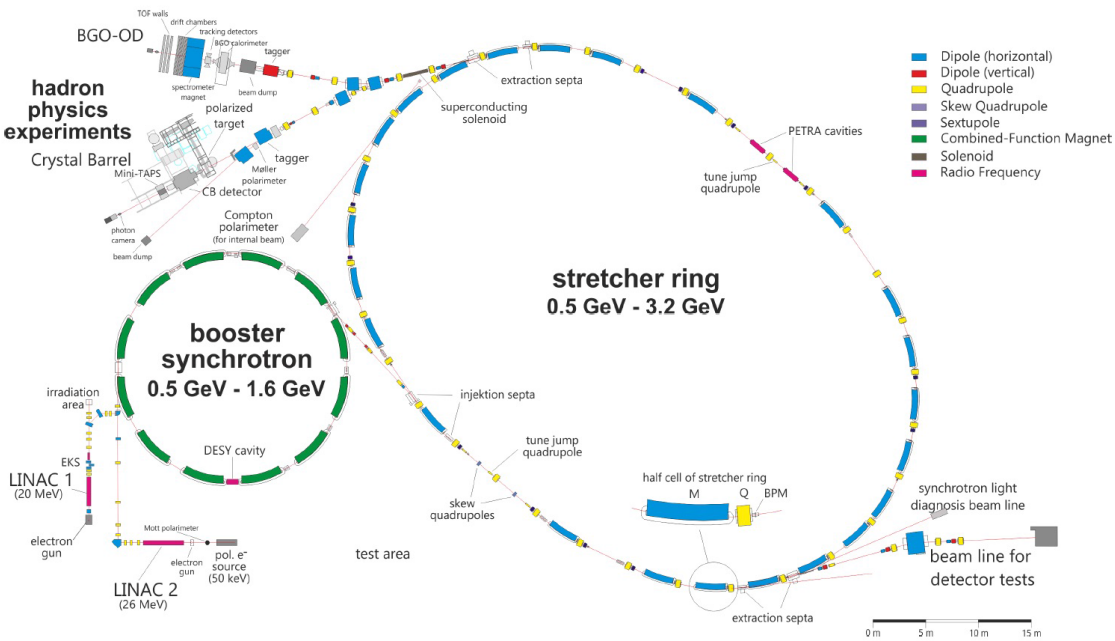

Figure 2.1: Overview of ELSA [8]

2.2 BGO-OD

The BGO-OD experiment - which can be seen in figure 2.2 - is fed with the electron beam provided by ELSA, which is then converted into a continuous energy-tagged bremsstrahlung photon beam. The generated photon beam is incident on a liquid hydrogen, liquid deuterium or solid target, allowing for meson photoproduction and the creation of residual ground as well as excited state baryons. The emerging particles then give rise to signals within the two main detector components, namely the central and forward detectors. These diverse components shall furthermore be explained in detail.

2.2.1 Tagging System

The purpose of the tagging system is determining the energy of a single bremsstrahlung photon by measuring the corresponding energy of the electron it originated from and providing the time reference for the BGO-OD experiment.

At first, the primary electron beam of ELSA with a given energy E_0 is irradiated onto a thin bremsstrahlung target - the radiator - which can precisely be aligned by the so-called goniometer. The electrons are being decelerated in the Coulomb field of the target nuclei, whereas approximately each single electron emits a single bremsstrahlung photon of energy E_γ. Hence, the energy of the bremsstrahlung photon can simply be determined by measuring the energy E_{e^-} of the electron that had been involved in the bremsstrahlung process:

$$E_\gamma = E_0 - E_{e^-}$$

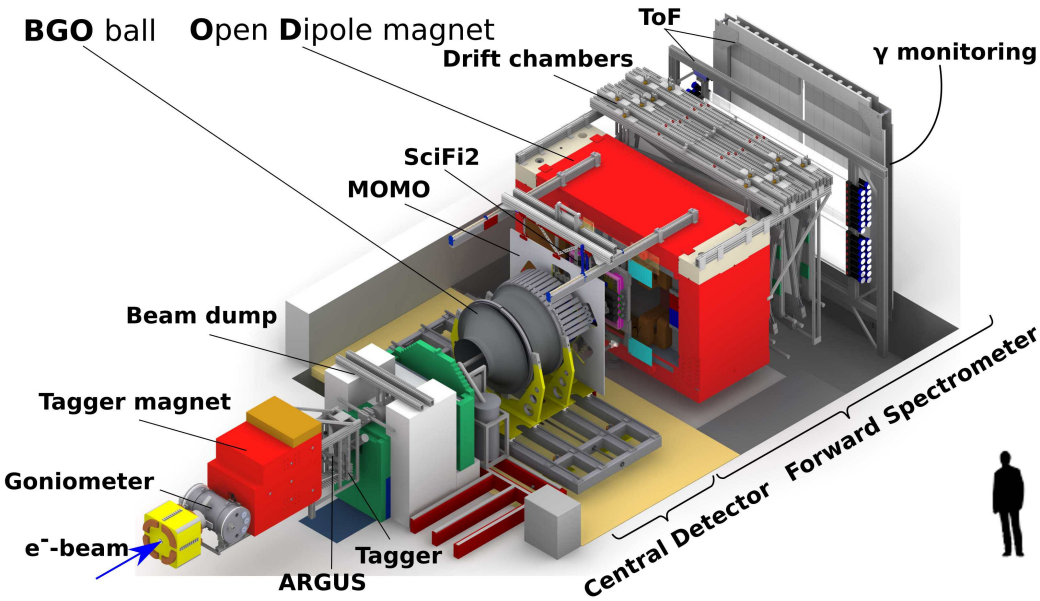

Figure 2.2: Overview of the BGO-OD experiment [10]

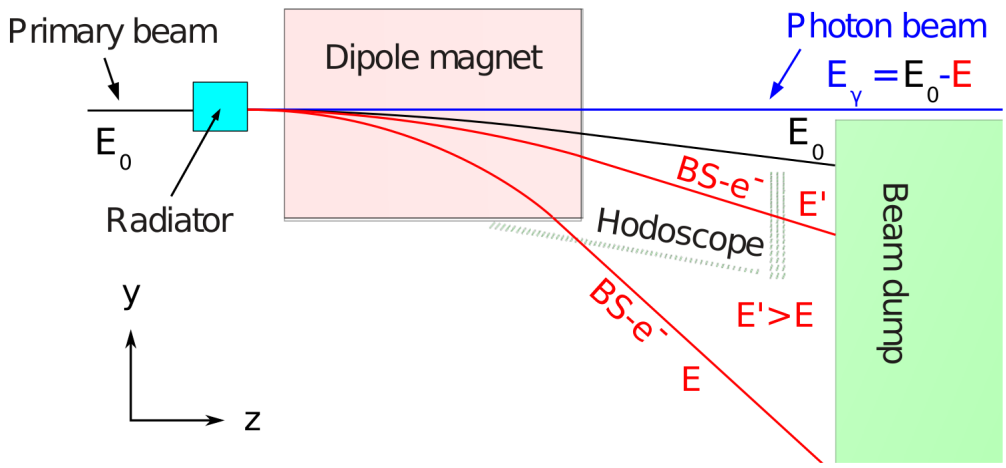

Figure 2.3: Overview of the tagger [11]

This can be achieved by using a magnetic spectrometer following the goniometer, as shown in figure 2.3. A post-bremsstrahlung electron traverses a dipole magnet and its trajectory is bend due to the Lorentz force, where the trajectory's radius depends on the electron momentum. Different radii lead to different impact points of the electrons on the position-sensitive hodoscope. The hodoscope consists of 120 plastic scintillators, which cover an energy range of $10\% E_0$ to $90\% E_0$. Out of the 120 plastic scintillators, 54 are positioned horizontally, whereas 66 had to be positioned vertically at a point where the focal plane of the dipole magnet lies within the beam dump, disabling a horizontal alignement.

Two adjacent scintillators overlap by 55% and are considered as a coincidence channel, providing the momentum of the post-bremsstrahlung electron. The energy width of a coincidence channel varies from $0.55\% E_0$ in the horizontal part to $0.80\% E_0$ - $2.12\% E_0$ in the vertical part. As the energy of the post-bremsstrahlung electron can be determined, the corresponding bremsstrahlung photon can be tagged with the correct energy. Non-interacting electrons are led to the beam dump. The hodoscope provides a time resolution of better than 120 ps and provides the time reference for the BGO-OD experiment [11].

The tagger is complemented by ARGUS, which is a scintillating fibre detector that enables a finer position resolution and therefore energy resolution, as each fibre covers a smaller region than the initial tagger scintillators. Additionally, ARGUS decreases the systematic error in the determination of the degree of linear polarization by one order of magnitude [12, 13].

At the end of the BGO-OD experiment, the Gamma Intensity Monitor (GIM) and the Flux Monitor (FluMo) are placed, which allow for a measurement of the collimated photon flux present at the target. GIM is a total absorbing Cerenkov detector whose usage is limited by photon rate and radiation damage. It is used to calibrate FluMo, which is a scintillating detector and measures only a part of the full flux, but up to very high rates. GIM and FluMo reduce the systematic error of the flux measurement to 5.7% [14].

2.2.2 Central Detector

The energy-tagged photons are collimated, led through a beam pipe and impinge on the target at the center of the BGO ball, which can be seen in figure 2.4. The central detector surrounds the target and provides energy as well as charge information of the traversing particles with a time resolution of about 3 ns. It is of special importance to this thesis, as the K^+ identification takes place inside the BGO calorimeter. It shall be described from inner layers to outer layers, starting with the target cell in the center.

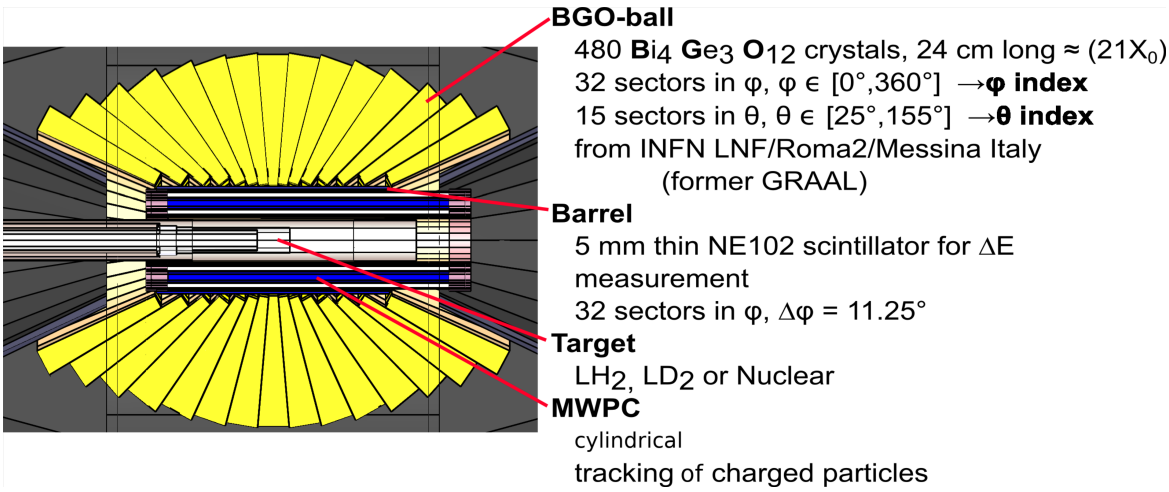

Figure 2.4: Slice view of the central detector [10]

The target cell can be filled with liquid hydrogen or liquid deuterium. Alternatively, a solid target such as carbon can be utilized. Currently, two types of target cells can be employed, one of 6 cm and one of 11 cm length. The front and back window of the target cell consist of a thin Mylar foil.

The target cell is surrounded by two cylindrical Multi-Wire Proportional Chambers (MWPCs), enabling the tracking of charged particles with a high angular resolution of about 1.7° [15].

Outside of the MWPCs, the scintillator barrel is positioned, being made up of a thin plastic layer. Comparing the fraction of energy ΔE deposited in the scintillator barrel with the energy deposited in the calorimeter, one can utilize the Bethe-Bloch equation to distinguish between charged and non-charged particles [16].

The scintillator barrel is surrounded by the BGO ball, which serves as the calorimeter of the central detector. It provides energy and direction information of the traversing particles by detecting their energy deposit. The BGO ball consists of 32 crystals in the azimuthal Φ sector, covering the full angular range, and 15 crystals in the polar Θ sector, covering a range from 25° to 155°. Each crystal is 24 cm long, corresponding to approximately $21X_0$ [10]. The BGO ball possesses a short timing resolution of about 3 ns. This is achieved by reading out the brief rising edge of the signal inside the bismuth germanate oxide using photomultiplier tubes fixed at the end of the crystals in combination with sampling ADCs [16]. The signal is read out separately for each single crystal. The K^+ identification is being carried out inside the BGO ball.

2.2.3 Forward Spectrometer

The forward spectrometer has not been utilized in this thesis and shall be covered for completeness. It detects charged particles with a θ angle of less than 10° - disregarding SciRi - and allows for momentum reconstruction, as the tracks of charged particles are measured before and after passing an open dipole magnet. Using time of flight walls, one can measure the velocity and reconstruct the particle's mass.

The acceptance gap between the central detector and the following components of the forward spectrometer is covered by the Scintillating Ring detector (SciRi). It can be utilized for time of flight measurements, as it provides a high detection efficiency and a time resolution of approximately 3 ns. It covers a θ range from 10° to 25° and consists of 96 plastic scintillator segments. The readout is carried out with avalanche photodiodes [10].

The particle's position and direction in front of the open dipole magnet are measured by MOMO and SciFi2, both scintillating fibre detectors. MOMO consists of six rotated, overlapping modules, whereas the fibres of SciFi2 are aligned horizontally and vertically [17].

The Open Dipole Magnet (OD) possesses a maximum magnetic field strength of $B_{max} = 0.53$ T and a bending power of $\int Bdl \approx 0.71$ T m [18].

Position and direction of charged particles that passed the open dipole magnet are measured with eight drift chambers that feature drift cells of hexagonal geometry. Two of the drift chambers are rotated by 90°, four of them by 9°, covering an area of 2.5 m $\times$ 1.2 m [19].

The Time of Flight Spectrometer (ToF) follows the drift chambers and consists of three walls that hold plastic scintillators horizontally. The horizontal position of traversing particles can be determined by analysing the time difference between the readouts of the two photomultiplier tubes that are placed at the ends of the scintillator. The vertical position is determined by the position of each individual scintillator itself. By using the timing information of the tagger, the velocity of a traversing particle can be determined. As the momentum is measured by the components of the forward spectrometer that have been mentioned beforehand, one can use these information to determine the corresponding mass and identify the particle [20].

CHAPTER 3

K^+ Identification

Commonly, K^+ are identified in tracking detectors, as it is non-trivial to distinguish them from other particles within calorimeters. In this thesis, a novel K^+ identification technique developed by Jude *et al.* [21] at the Crystal Ball experiment at MAMI, Mainz, was applied. The technique enables an identification of the K^+ inside the BGO ball by utilizing the fact that the K^+ decays weakly inside the calorimeter, depositing two distinct time-delayed energy clusters inside adjacent crystals. By putting cuts on energy deposit and the time span between clusters, one can distinguish K^+ from other particles. This technique benefits from the high time resolution of 3 ns inside the BGO ball and the separate readout per crystal.

The K^+ has a lifetime of (12.380 ± 0.020) ns [22], the main decay modes are:

- $K^+ \rightarrow \mu^+ \nu_\mu$, BR=(63.56 ± 0.11)%
- $K^+ \rightarrow \pi^+ \pi^0$, BR=(20.67 ± 0.08)%

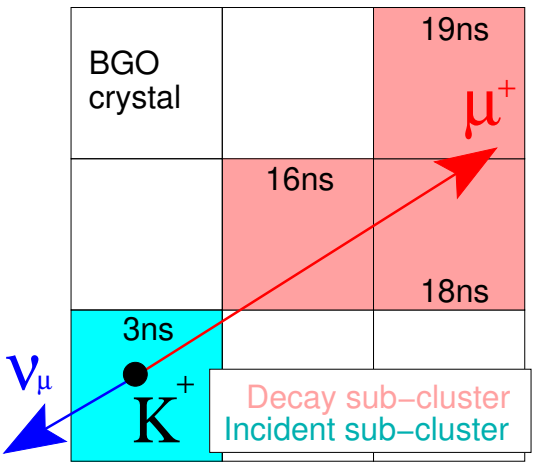

Figure 3.1: Schematic of the BGO crystals and the clustering process of a muonic decay as seen from the point of view of the target center [23]

Figure 3.1 shows a scheme of the BGO crystals seen from the point of view of the target center. The

K^+ decays at rest into a μ^+ and a ν_μ, in most cases depositing its full energy in a single crystal due to Bethe-Bloch energy loss. The uncharged ν_μ leaves the crystal without a trace back-to-back to the μ^+, which deposits fractions of its energy in the adjacent crystals it traverses. The energy cluster originating from the K^+ is called the incident sub-cluster (ISC), whereas the energy cluster originating from the μ^+ is depicted as the decay sub-cluster (DSC). The K^+ identification is reliant on the correct assignement of each single hit in the BGO crystals to the correct cluster. In order to identify a particle as a K^+, one has to apply several cuts to the data aquired by the BGO ball:

- The restraints on the ISC are as follows:
  - The ISC consists of one single hit only, as the detection probability for hits in multiple neighboring crystals is very low
  - There are no other hits within 8 ns of the first hit
  - The energy deposit is greater than 50 MeV
- The restraints on the DSC are as follows:
  - The cluster consists of at least three hits
  - The time span between two successive hits is less than 8 ns
  - The summed energy deposit is greater than 50 MeV
  - The cluster contains hits that are bordering the hit from the ISC
  - The fractional energy in the furthest hit of the DSC compared to the full energy of the DSC is lower than 5%. This property is depicted as 'decay energy localisation'
  - The average difference in angle between each crystal in the DSC and ISC is lower than 40°. This property is depicted as 'decay cluster linearity'

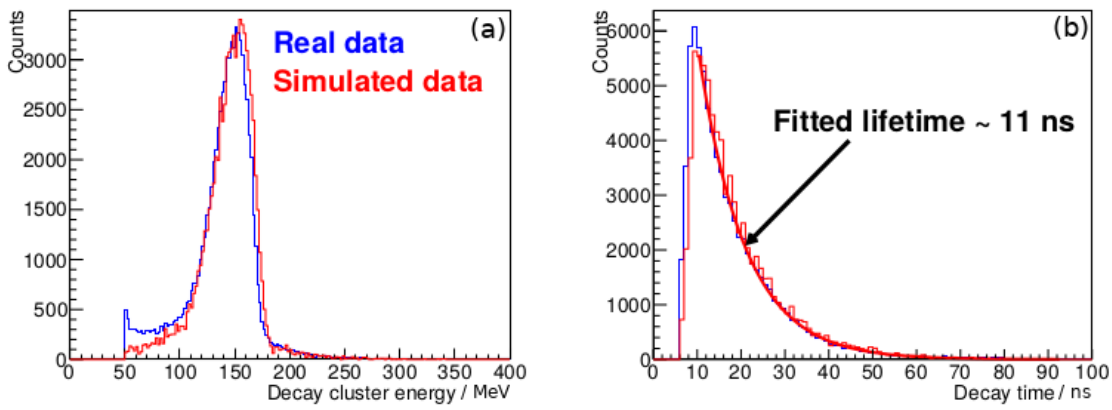

Figure 3.2: Muonic decay cluster characteristics for experimental data (blue) and simulated data (red): (a) DSC energy sum (b) Time difference between the ISC and DSC [23]

The DSC energy sum of the muonic decay mode can be seen in figure 3.2 (a), showing good agreement between real and simulated data. A peak at 150 MeV can be observed, which corresponds to the energy of the μ^+ from the muonic decay of the K^+ at rest. Figure 3.2 (b) shows the time difference

between the ISC and DSC decreasing exponentially with a lifetime of ~11 ns, which is expected for the K^+.

Two parameters were used to distinguish between the two dominant K^+ decay modes: The so-called decay energy localisation, depicting the fractional energy in the furthest hit of the DSC compared to the full energy of the DSC, and the decay cluster linearity, depicting the average difference in angle between each crystal in the DSC and ISC. These two parameters were chosen by iterative trial and error to minimize the contribution of the pionic decay to the observed signal. A small fraction of pionic and other decay modes, such as $K^+ \rightarrow \pi^0 e^+ \nu_e$ with a branching ratio of 5%, are unremovable from the data set and remain in the yield. Finally, minor energy corrections are applied in order to match real data to simulated data.

Having identified the K^+, one can employ the DSC energy sum and perform a $\Delta E - E$ analysis, where the ΔE information are gained from the scintillator barrel, to reconstruct the momentum of the K^+ [21].

The following chapter describes how the data was handled once the K^+ were identified.

CHAPTER 4

Analysis

4.1 Overview

Pronounced dip structures between $K^*\Lambda$ and $K^*\Sigma$ thresholds in $K_S^0\Sigma^+$ photoproduction off the proton are in good accordance with pentaquark models based on vector meson-baryon interactions that were able to predict the recently discovered LHCb pentaquark states in the hidden charm sector [5, 6]. Thus, the strange sector might be explicable by meson-meson and meson-baryon quark models analogously to the charm sector. More fundamental research in the strange sector is needed to resolve this issue. The goal of this thesis is the measurement of the differential cross section of the reaction $\gamma n \rightarrow K^+\Sigma^-$, providing complementary data with greater statistical precision to the existing CLAS data set.

This subchapter shall give an overview of the general analysis procedure, whereas the following subchapters shall focus on each individual step.

The differential cross section can be determined through:

$$(\frac{d\sigma}{d\Omega})_{K^+\Sigma^-} = \frac{N_{K^+\Sigma^-}}{N_\gamma \rho_n \epsilon(E_\gamma, \theta)\Omega} \tag{4.1}$$

with

$N_{K^+\Sigma^-}$: Number of measured $\gamma n \rightarrow K^+\Sigma^-$ reactions
N_γ : Integrated photon flux
ρ_n : Neutron area density of the target
$\epsilon(E_\gamma, \theta)$: Detection efficiency, depending on beam energy E_γ and angle θ
Ω : Solid angle element

Trivially, such a thing as a pure neutron target does not exist, implying the use of a liquid deuteron target. As the momentum transfer of the incident photon beam is much greater than two times the Fermi momentum of the deuteron, we do not observe coherent reactions with the deuteron as a whole, but incoherent reactions with the constitutent proton and neutron. Thus, the differential cross section of the reactions off the deuteron can be described as the incoherent sum of the differential cross

sections of those off the proton and neutron, respectively, as illustrated in figure 4.1:

$$\frac{d\sigma}{d\Omega_d} = \frac{d\sigma}{d\Omega_p} + \frac{d\sigma}{d\Omega_n}$$
$$\Leftrightarrow \frac{d\sigma}{d\Omega_n} = \frac{d\sigma}{d\Omega_d} - \frac{d\sigma}{d\Omega_p}$$

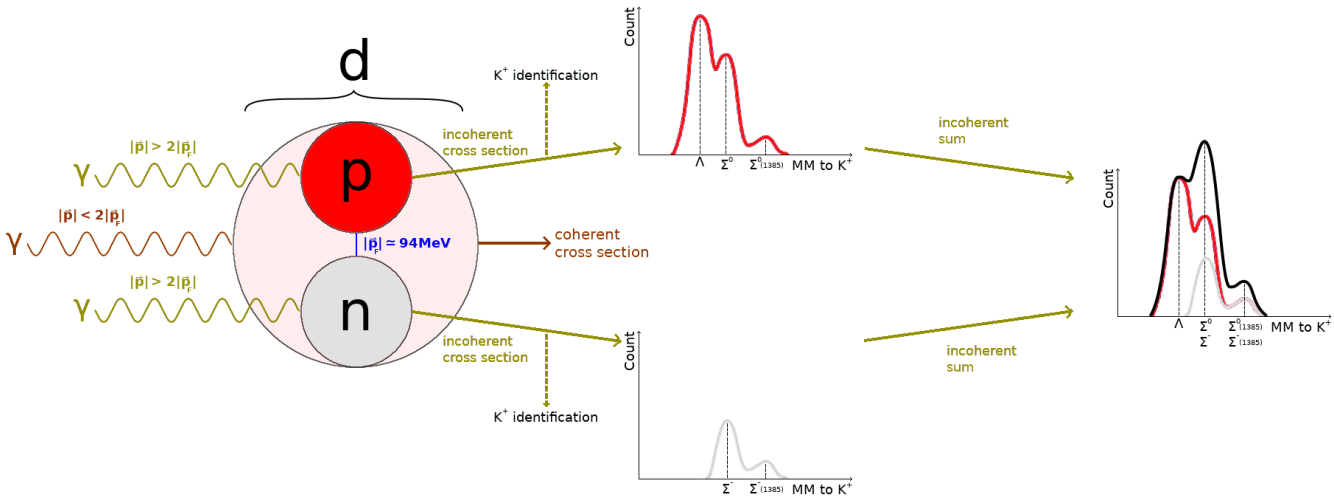

Figure 4.1: Illustration of the composition of the observed cross section. Using a deuterium target and high momentum transfer, we observe the incoherent sum of cross sections (black spectrum) of the reaction channels off the proton (red spectrum) and neutron (gray spectrum), respectively

The reaction channels off the proton are:

$$\begin{aligned}\gamma p \rightarrow & K^+\Lambda \\ & K^+\Sigma^0 \\ & K^+\Sigma^0(1385)\end{aligned}$$

Contrary, the reaction channels off the neutron are:

$$\begin{aligned}\gamma n \rightarrow & K^+\Sigma^- \\ & K^+\Sigma^-(1385)\end{aligned}$$

The K^+ are identified according to chapter 3. As one cannot distinguish directly between those reactions when using a deuteron target, one must get rid of the proton contribution indirectly. This can be achieved by employing a liquid hydrogen target, measuring the number of reactions off the proton $N_{p'}$ and subtracting from the number of reactions off the nucleons inside the deuteron $N_d = N_{n+p}$, while taking care of normalization factors for integrated photon flux and target area density as well as the Fermi momentum of the nucleons inside the deuteron, as expressed in equation 4.2.

$$\frac{N_n}{\rho_d N_{y_d}} = \frac{N_d}{\rho_d N_{y_d}} - \frac{N_{p'}}{\rho_{p'} N_{y_{p'}}} \tag{4.2}$$

Note that inside a deuteron target, $\rho_d = \rho_n = \rho_p$. The number N_n includes two reaction channels of the neutron, namely

$$N_n = N_{K^+\Sigma^-} + N_{K^+\Sigma^-(1385)} \tag{4.3}$$

One can attempt to distinguish between those reaction channels by measuring the missing mass to the K^+ and fitting to the two peaks that are visible in the spectrum.
Finally, the detection efficiency $\epsilon(E_\gamma, \theta)$ depending on energy and angle must be determined. As the solid angle element Ω is known, the differential cross section can then be determined using equation 4.1.

4.2 Fermi Momentum Correction

The deuteron is a bound state of a proton and a neutron. As both of these particles are fermions, they obey Fermi statistics and possess a Fermi momentum of about $|\vec{p}|_\mathrm{F} = 94\,\mathrm{MeV}$. One model describing the corresponding nucleon-nucleon interaction has been derived by Machleidt, Holinde and Ester in 1987 in the so-called 'Bonn model' [24].

In the Bonn model, the forces between nucleons are mediated by field-theoretical meson exchange. The interaction part of the corresponding Hamiltonian consists of N-N-meson and N-Δ-meson contributions, where different mesons are responsible for nuclear forces at different ranges.
The long-range (distance between nucleon center: $r \geq 2\,\mathrm{fm}$) tensor force as well as the short-range ($r \leq 1\,\mathrm{fm}$) repulsion and spin-orbit force are provided by the well-known one-meson-exchange contributions from π and ω. The intermediate-range ($1\,\mathrm{fm} < r < 2\,\mathrm{fm}$) is dominated by 2-$\pi$-exchange, taking resonances and direkt π-π-interactions into account.

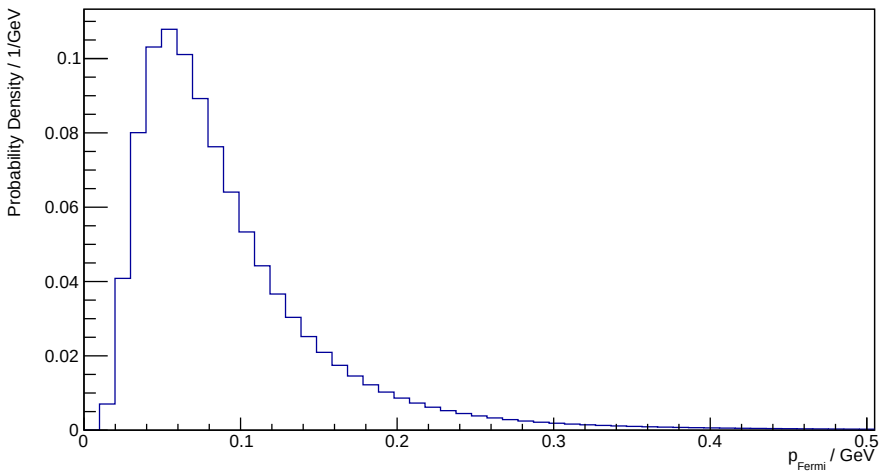

Figure 4.2: Probability distribution of the Fermi momentum inside the deuteron

According to the Bonn model, the Fermi momentum of the nucleons inside the deuteron is not a fixed value, but is a value that underlies a certain probability distribution, which is shown in figure 4.2.

In order to get rid of the background channels that originate from photoproduction off the proton inside the deuteron, the same K^+ identification technique that was used for the liquid deuteron target was used for a liquid hydrogen target. Most of the background will be eradicated by subtracting the obtained missing mass to the K^+ of the hydrogen target from the obtained missing mass to the K^+ of the deuteron target. However, in contrast to the proton within the deuteron, liquid hydrogen is not part of a bound state of nucleons and does not possess any corresponding Fermi momentum, which makes a direct subtraction of the two data sets impossible. The hydrogen data must therefore be corrected before subtraction.

The Fermi momentum correction for the liquid hydrogen data set is obtained by drawing a random probability-weighted entry from the probability distribution of the Fermi momentum and adding the corresponding four vector to the four vector of the target for each event. This simulates a liquid hydrogen target that possesses an artificial Fermi momentum analogous to that of the proton inside the deuteron.

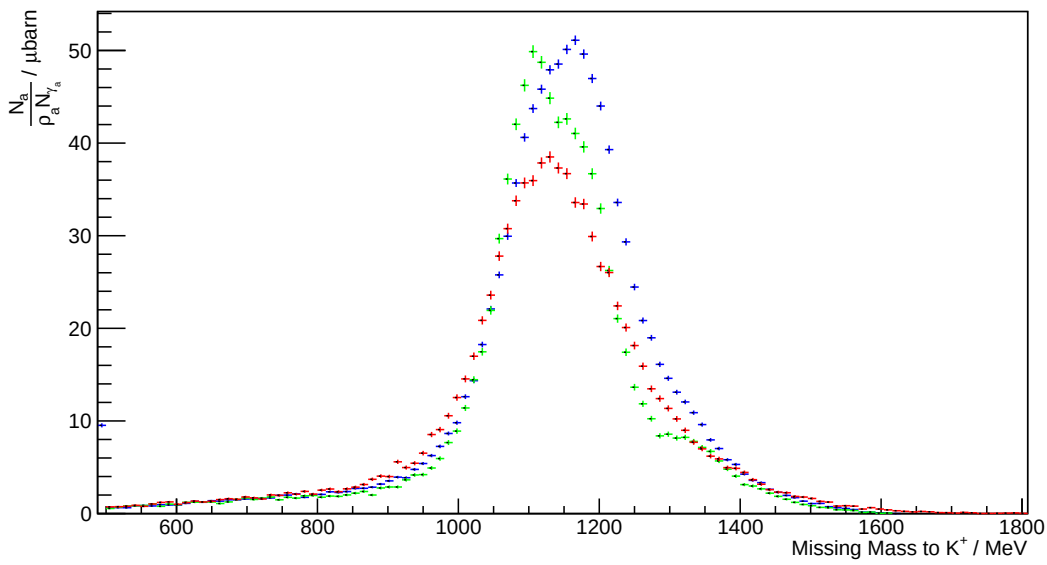

Figure 4.3: Missing mass to the K^+ for the deuteron target (blue), for the proton target without Fermi momentum correction (green) and with Fermi momentum correction (red). The integral of the data set with Fermi momentum correction differs from that without correction by 1.23%, as the data include a punch-through cut described in the next chapter

Figure 4.3 shows the missing mass to the K^+ for the deuteron target (blue), the proton target without Fermi momentum correction (green) and with Fermi momentum correction (red). The relation of the deuteron data set and the proton data set without Fermi momentum correction is as expected, the deuteron data shows a higher count at missing masses near Σ^- and $\Sigma^-(1385)$. At the rising edge, the peak of the proton data set with Fermi momentum correction is slightly broader than the peak of the deuteron data set. For comparison, the proton data set has also been broadened using a Gaussian

distribution instead of the Bonn model's Fermi momentum distribution. Modeling a rising edge similar to that of the deuteron data, the maximum count of the proton data appeared to be too high in this case. Thus, the correction with the Bonn model's Fermi momentum distribution appears to be the best option and is employed for further analysis.

4.3 Punch-through Correction

The Bethe-Bloch energy loss of the K^+ inside the BGO calorimeter allows for an assignement of energy and momentum to the corresponding K^+. However, high-energetic K^+ might penetrate the BGO crystals deep enough so that they decay right in front of the photomultiplier tubes, which are fixed at the back of each crystal - this event is depicted as 'punch-through'. Comparing simulated data to real data shows that punch-through events cause issues regarding the readout of the signal, leading to a flawed assignement of energy. K^+ that punched through are misidentified as lower-energetic ones. It might be possible that the μ^+ originating from the K^+ decay leave the crystals at their backs, depositing only a fraction of their true energy within it.

The kinetic energy at which the punch-through occurs is $E_{\text{pt}} = 420\,\text{MeV}$. As the angle θ_{LAB} of the K^+ is measured correctly - whether it punches through or not - and as we observe a two-body reaction, one can utilize this information and four momentum conservation to calculate the true kinetic energy of the K^+:

$$p_\gamma + p_{\text{target}} = p_{K^+} + p_{\Sigma^-} \tag{4.4}$$

$$E_{K^+}^{\text{kin}} = \frac{AE_{\text{initial}} + |\vec{p}_{\text{initial}}| \cos(\theta_{\text{LAB}})\sqrt{A^2 - 4m_{K^+}^2(E_{\text{initial}}^2 - |\vec{p}_{\text{initial}}|^2 \cos(\theta_{\text{LAB}})^2)}}{2(E_{\text{initial}}^2 - |\vec{p}_{\text{initial}}|)} - m_{K^+} \tag{4.5}$$

with

$$\begin{aligned} E_{\text{initial}} &= E_{\text{target}} + E_\gamma \\ \vec{p}_{\text{initial}} &= \vec{p}_{\text{target}} + \vec{p}_\gamma \\ A &= E_{\text{initial}}^2 + m_{K^+}^2 + -\vec{p}_{\text{initial}}^2 - m_{\Sigma^-}^2 \end{aligned}$$

The full derivation is shown in appendix B. When the calculated kinetic energy $E_{K^+}^{\text{kin}}$ is greater than or equal to E_{pt}, the registered K^+ has punched through the crystal and is sorted out. Note that due to the Fermi motion, $\vec{p}_{\text{target}}$ is unequal to zero. For the proton target, the Fermi momentum has been created artificially as described in the previous subchapter, therefore $\vec{p}_{\text{target}}$ is known for each single event. For the deuteron target, this is not the case. Hence, $\vec{p}_{\text{target}}$ has been set to zero and a systematic error analysis has been carried out. Comparison with a mean value of $|\vec{p}|_{\text{target}} = 94\,\text{MeV}$ lead to a systematic error of 11.1%. As can be seen in figure 4.4 and 4.5, the correction gets rid of flawed data points quite effectively. Parts of the signal that were smeared out towards higher energies are being cut off.

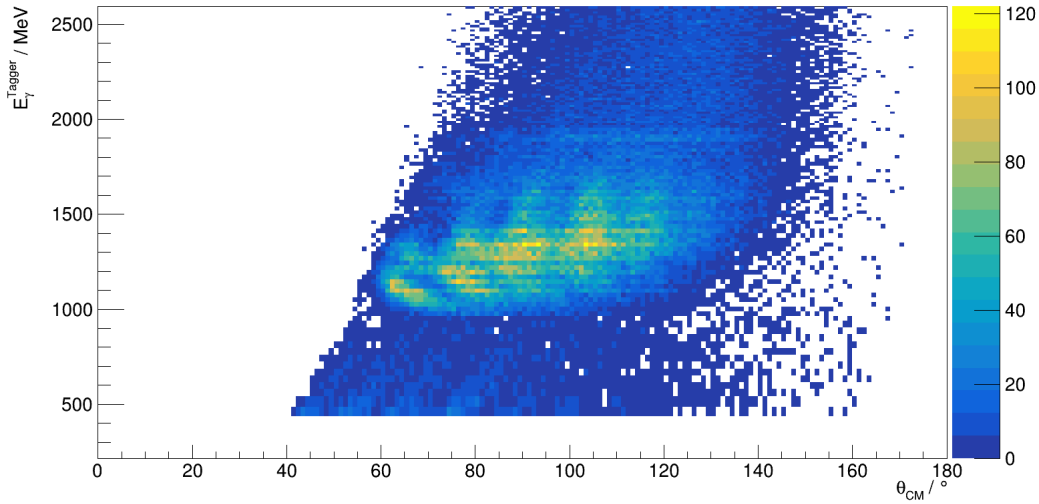

Figure 4.4: Tagger energy E_γ^{Tagger} versus center-of-mass angle θ_{CM} without punch-through correction. The signal is smeared out towards higher energies

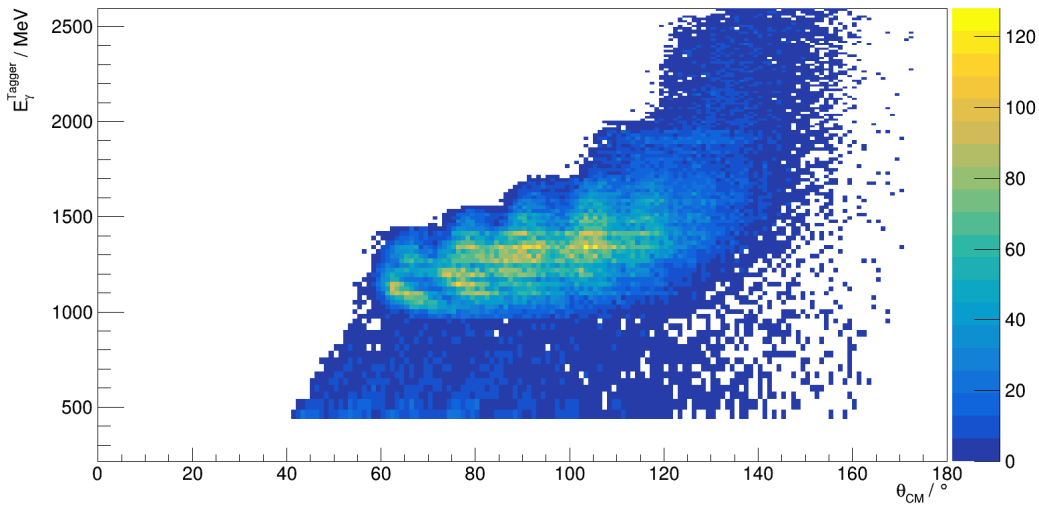

Figure 4.5: Tagger energy E_γ^{Tagger} versus center-of-mass angle θ_{CM} with punch-through correction. The correction gets rid of the parts of the signal that were smeared out towards higher energies

4.4 Integrated Photon Flux

Trivially, the differential cross section depends on the number of incident photons. As we are handling two data sets with different integrated photon flux, we need to normalize these data sets before subtraction. The tagging system described in section 2.2.1 provides us with precise energy information of the incident beam. Figure 4.6 shows the integrated photon flux F as a function of beam energy E_γ,

decreasing with $\frac{1}{E_\gamma}$.

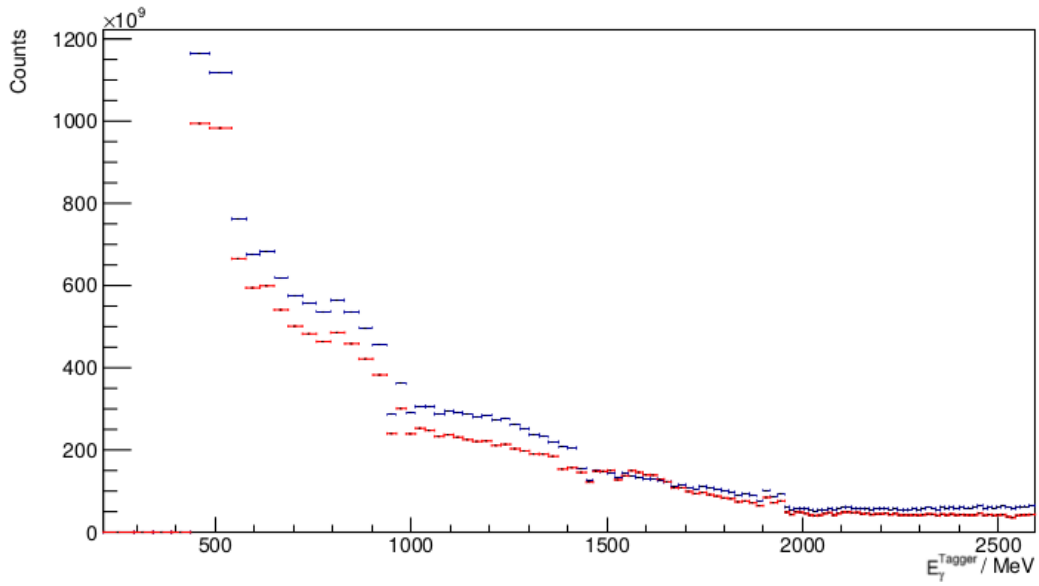

Figure 4.6: Integrated photon flux for proton target (red) and deuteron target (blue) depending on beam energy

The normalization is plainly achieved by dividing the number of identified K^+ at certain beam energies by the integrated photon flux $F(E_\gamma)$ at that energy, all while taking care of the corresponding statistical errors.

4.5 Target Area Density

In order to determine the differential cross section, one must know the neutron target area density. Therefore, the proton and deuteron data sets are normalized before subtraction by dividing the number of identified K^+ by the target area densities, which are equal to the target densities times the target length. Both beamtimes used target cells with a length of $l = (11.1 \pm 0.1)\,\mathrm{cm}$. The target densities of liquid hydrogen and liquid deuterium are similar, but not equal. Table 4.1 shows the used target densities [25].

Material	Nucleus density $\left(\frac{1}{\mathrm{m}^3}\right)$	Proton density $\left(\frac{1}{\mu\mathrm{b}\cdot\mathrm{cm}}\right)$	Neutron density $\left(\frac{1}{\mu\mathrm{b}\cdot\mathrm{cm}}\right)$
Liquid hydrogen	4.237×10^{28}	4.237×10^{-8}	0
Liquid deuterium	5.053×10^{28}	5.053×10^{-8}	5.053×10^{-8}
Mylar foil	6.403×10^{28}	4.136×10^{-7}	4.111×10^{-7}

Table 4.1: Nucleus, proton and neutron densities for different materials [25]

The front and back windows of the employed target cell consist of Mylar foil, possessing a proton density about one order of magnitude higher than that of liquid hydrogen and liquid deuterium. The investigation of the effect of the Mylar foil on the analysis exceeds the extent of this master thesis and will not be taken into account.

4.6 Subtraction of Data Sets

After having applied the Fermi momentum and punch-through corrections as well as the integrated photon flux and target area density normalizations, one can subtract the proton data set from the deuteron data set according to equation 4.2:

$$\frac{N_n}{\rho_d N_{y_d}} = \frac{N_d}{\rho_d N_{y_d}} - \frac{N_{p'}}{\rho_{p'} N_{y_{p'}}} \tag{4.2}$$

The resulting missing mass spectrum to the K^+ over the full energy and angular range can be seen in figure 4.7. The data set that is a result of the subtraction shall be depicted as 'subtraction data set'.

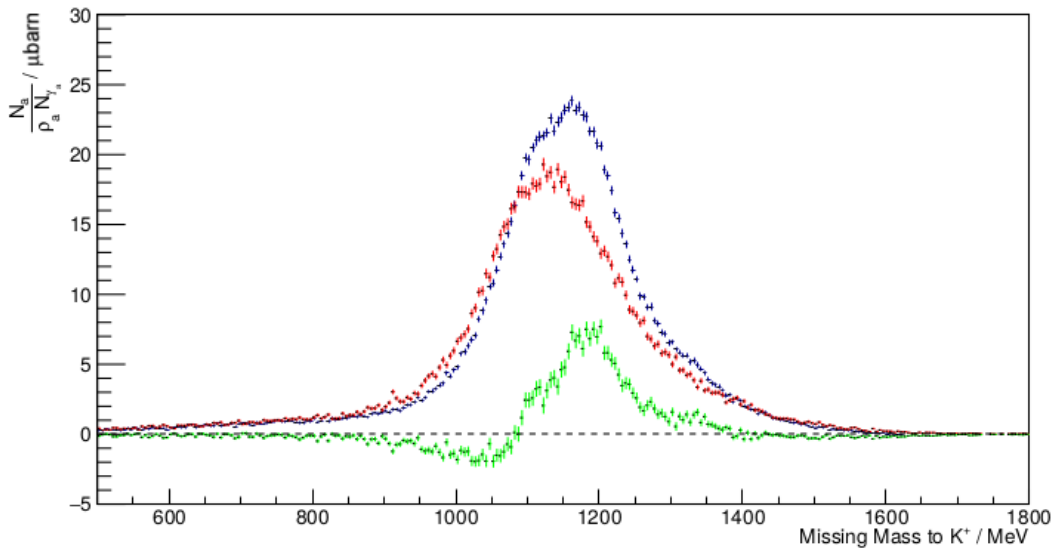

Figure 4.7: Missing mass to the K^+ for the Fermi-broadened proton data set (red), deuteron data set (blue) and subtraction data set (green) over the full energy and angular range

It is noticeable that the subtracion data set possesses negative entries until an energy of about 1 100 MeV. This implies that the Fermi momentum correction of the proton data set has been overestimated with regard to the width of the momentum distribution, broadening the missing mass spectrum to the K^+ too extensively. It shall be stated at this point of the analysis that chapter 4.8 will show that this effect is non-critical for the end result.

We are interested in the differential cross section depending on beam energy and center-of-mass angle.

The missing mass to the K^+ is therefore being investigated for single energy and $\cos(\theta_{\mathrm{CMS}})$ bins, as exemplarily shown in figure 4.8. Studying figure 4.8, one would expect a continuous spectrum, but regions without any counts are visible. These gaps are caused by the fact that during the K^+ identification, we limited the identification of the incident sub-cluster to hits in a single crystal only, as the detection probability for hits in multiple crystals was very low, leading to a discretization of the available angular range. The gaps vary position dependent on the observed energy range. Thus, what appear to be peaks in the missing mass spectrum can not directly be identified as single particles, but as an artificial structure caused by the angular discretization. Fortunately, this structure can be recreated in simulations, enabling us to use Roofit in order to attempt to distinguish between Σ^- and $\Sigma^-(1385)$.

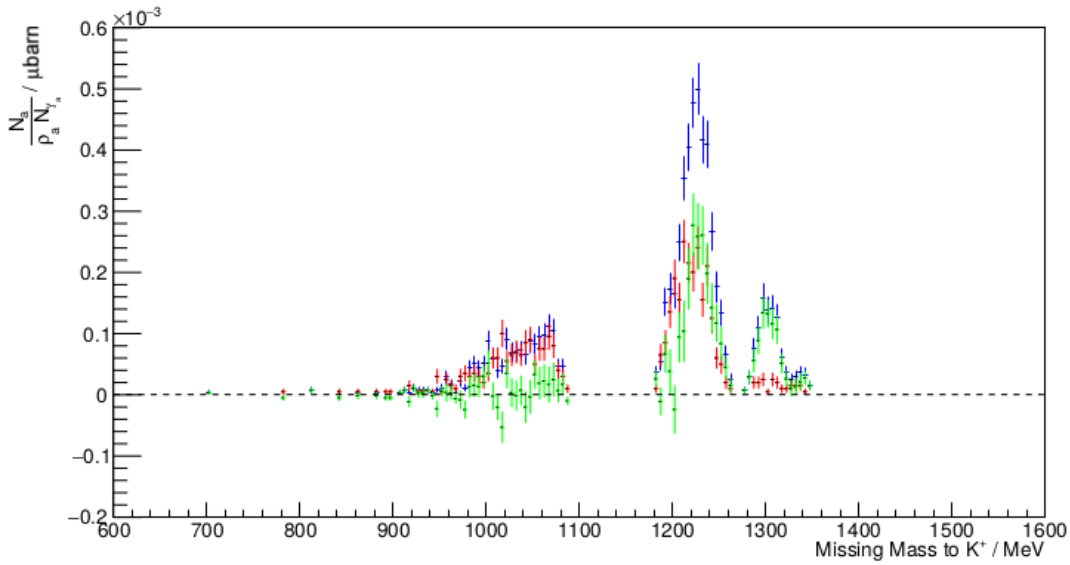

Figure 4.8: Missing mass to the K^+ for the Fermi-broadened proton data set (red), deuteron data set (blue) and subtraction data set (green) for $E = (1358.515 \pm 30.140)$MeV and $\cos(\theta) = -0.15 \pm 0.5$. The gaps within the spectrum are a result of angular discretization

4.7 Dissection of $K^+\Sigma^-$ and $K^+\Sigma^-(1385)$

At this point of the analysis, we got rid of the background originating from photoproduction off the proton. However, the contribution of $K^+\Sigma^-(1385)$ originating from photoproduction of the neutron has remained in the subtraction data set and shall be examined in this chapter.

The contribution of $K^+\Sigma^-(1385)$ has been investigated by simulating the decays $\gamma n \rightarrow K^+\Sigma^-$ and $\gamma n \rightarrow K^+\Sigma^-(1385)$, then feeding those simulated data and the real subtraction data set to Roofit, which adjusts the heigths of the simulated spectra so that the sum fits the real data in an optimal way.

Figure 4.9 shows an energy and angular range in which Roofit seems to succeed in fitting to

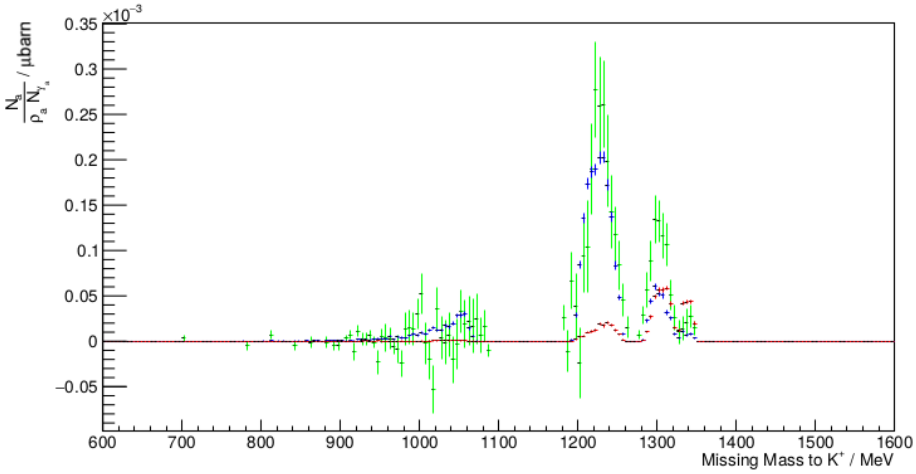

Figure 4.9: Roofit for $E = (1358.515 \pm 30.140)$MeV and $\cos(\theta) = -0.15 \pm 0.5$, showing real data (green), fitted $K^+\Sigma^-$ spectrum (blue) and fitted $K^+\Sigma^-(1385)$ spectrum (red). Roofit seems to succeed in fitting to the real data

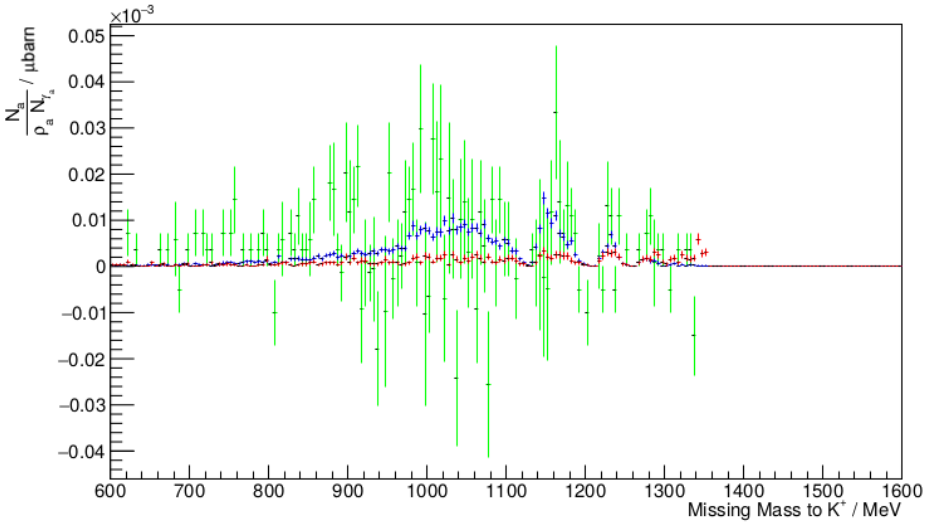

Figure 4.10: Roofit for $E = (1358.515 \pm 30.140)$MeV and $\cos(\theta) = -0.75 \pm 0.5$, showing real data (green), fitted $K^+\Sigma^-$ spectrum (blue) and fitted $K^+\Sigma^-(1385)$ spectrum (red). Roofit seems to deliver questionnable fits when confronted with large relative errors as well as negative entries

the real data, while figure 4.10 shows a range where the relative error size of the real data points is quite large, making the fit of the simulated spectra questionable.

Generally speaking, Roofit seems to have problems with fitting to spectra with large relative error ranges and which contain negative entries, as the simulated data are always positive. It can be assumed that the fraction of $\Sigma^-(1385)$ of the spectrum is quite small compared to the fraction of Σ^-. A more sophisticated dissection of the $\Sigma^-(1385)$ contribution surpasses the extent of this thesis. We will therefore consider the $\Sigma^-(1385)$ contribution to be negligible.

4.8 Number of Measured $\gamma n \rightarrow K^+\Sigma^-$ Reactions

As we considered the contribution of $\Sigma^-(1385)$ to be negligible, there is no need to distinguish between different decay channels in the subtraction data set anymore and fits to the missing mass spectrum become irrelevant. For each combination of beam energy and angle, we can therefore take the full integral in order to determine $\frac{N_{K^+\Sigma^-}}{\rho_d N_{\gamma_d}}$. At some points in the missing mass spectrum, negative entries occur. Those entries are the result of the subtraction of the Fermi-broadened proton data set. The Fermi broadening in combination with the punch-through cut altered the full integral of the original proton data set by only 1.23%, we can therefore assume it stayed approximately constant. Due to the subtraction, a decreased count at some point in the missing mass spectrum of the subtraction data set, even a negative count, corresponds to an increased count at another point in the spectrum. This allows us to integrate over negative entries and still yield valid results for the number of measured $\gamma n \rightarrow K^+\Sigma^-$ reactions.

It is worth mentioning that the data was binned in $\cos(\theta_{\mathrm{CMS}})$ with a bin size of 0.1, so the solid angle element is $\Omega = 2\pi \cdot 0.1$.

4.9 Simulated Detection Efficiency

The passage of particles through matter can be simulated by using Geant4. The software includes a complete range of functionalities such as tracking, taking detector geometry into account, employing different physics models and hit detection[26]. It was utilized to simulate 10^8 events of $\gamma n \rightarrow K^+\Sigma^-$. The K^+ identification method appeared to function analogously for real and simulated data. The simulated detection efficiency ϵ depending on beam energy E_γ and observed angle $\cos(\theta_{\mathrm{CMS}})$ could be determined by dividing the simulated events that were detected by the simulated detector by all events that were fed to the simulated detector as an input.

$\epsilon(E_\gamma, \cos(\theta_{\mathrm{CMS}}))$ can be seen in figure 4.11, obtaining a maximum of 6% at $\cos\theta_{\mathrm{CMS}} \approx -0.3$ and $E_\gamma \approx 1\,350\,\mathrm{MeV}$. It then predominantely decreases towards combinations of backward angles and small energies as well as towards combinations of forward angles and high energies. In some areas, the simulated detection efficiency is close to, but still above zero. Dividing background counts by a tiny simulated detection efficiency would lead to a false increase in differential cross section. To minimize the impact of the background signal on the differential cross section, a minimum threshold has been applied to the simulated detection efficiency, discarding all events that possess a simulated detection efficiency of below 1%. This can be seen in figure 4.12.

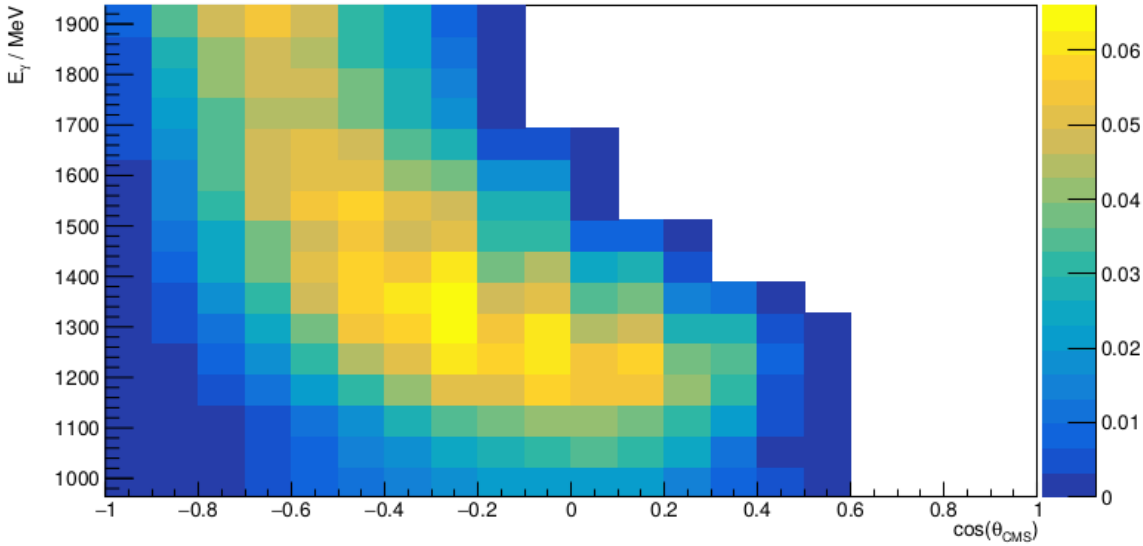

Figure 4.11: Simulated detection efficiency for $\gamma n \rightarrow K^+\Sigma^-$ without minimum threshold

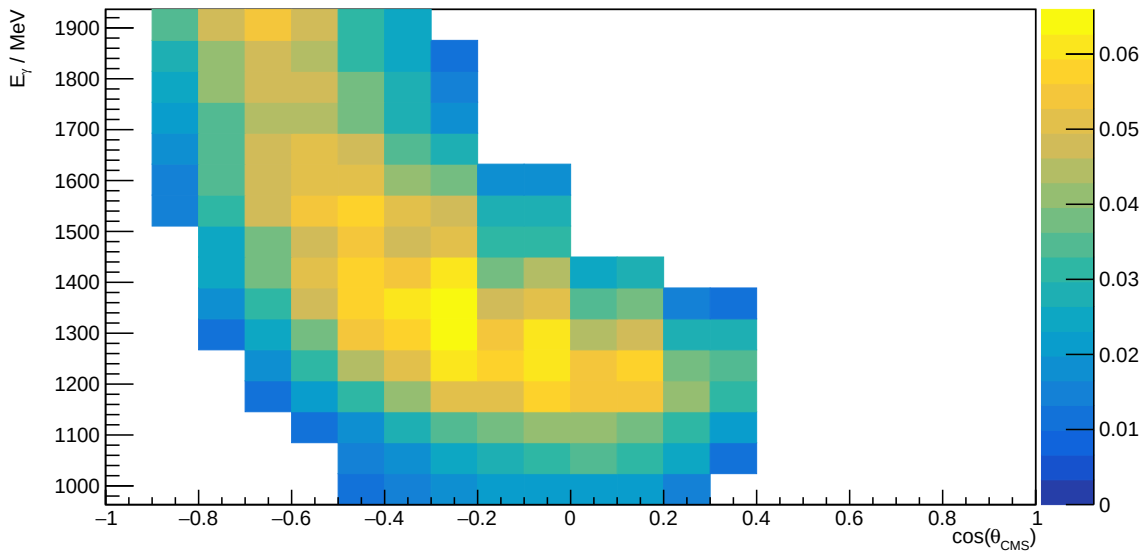

Figure 4.12: Simulated detection efficiency for $\gamma n \rightarrow K^+\Sigma^-$ with minimum threshold of 1%

CHAPTER 5

Results

In the preceding chapters we were able to obtain all necessary parameters required to finally specify the differential cross section $(\frac{d\sigma}{d\Omega})(E_\gamma, \cos(\theta_{\mathrm{CMS}}))$ depending on beam energy E_γ and observed angle $\cos(\theta_{\mathrm{CMS}})$, making use of equation 4.1:

$$(\frac{d\sigma}{d\Omega})_{K^+\Sigma^-} = \frac{N_{K^+\Sigma^-}}{N_\gamma \rho_n \epsilon(E_\gamma, \theta)\Omega} \tag{4.1}$$

The results are shown in figure 5.1, plotted together with data from CLAS [7].

For an angle of $\cos(\theta_{\mathrm{CMS}}) = -0.85$, the signal starts at an energy of $E_\gamma = 1\,540\,\mathrm{MeV}$ and expands to higher energies, showing a differential cross section that fluctuates around 0.027 µb by about ±0.010 µb.

For the following more forward angles, the differential cross section in this energetic region rises, until it reaches a mean value of 0.061 µb at $\cos(\theta_{\mathrm{CMS}}) = -0.55$. In addition to that, for the same angles, we gain more acceptance and thus more signal towards lower energies. For $\cos(\theta_{\mathrm{CMS}}) = -0.75$ and $\cos(\theta_{\mathrm{CMS}}) = -0.65$, these parts of the signal show an overly increase in differential cross section compared to the rest of the signal.

At $\cos(\theta_{\mathrm{CMS}}) = -0.45$, the signal starts at $E_\gamma = 993\,\mathrm{MeV}$ with a differential cross section of 0.015 µb, rising up to 0.075 µb at $E_\gamma = 1\,358\,\mathrm{MeV}$. It then stays approximately constant, until it shows greater fluctuation from $E_\gamma = 1\,783\,\mathrm{MeV}$ on upwards.

For the subsequent more forward angles, the shape of the cross section remains similar for low energies, but we loose acceptance and therefore data points for high energies. For high energies, the differential cross section generally declines, leading to a bump-like shape being especially prominent at $\cos(\theta_{\mathrm{CMS}}) = -0.25$. However, it also possesses greater fluctuations and errors than the data for low energies.

Finally, for $\cos(\theta_{\mathrm{CMS}}) = 0.35$, there are only a few data points left, fluctuating around 0.06 µb.

The obtained data shows good agreement with the CLAS data. It utilizes a finer energy binning and generally inherits much smaller error ranges. From $\cos(\theta_{\mathrm{CMS}}) = -0.85$ to $\cos(\theta_{\mathrm{CMS}}) = -0.35$, the measured cross section matches the one by CLAS satisfyingly well, mostly lieing within error range. Deviations from the CLAS data manifest themselves in the following way: At $\cos(\theta_{\mathrm{CMS}}) = -0.25$ and more forward angles, the differential cross section declines for high energies to an extent that no

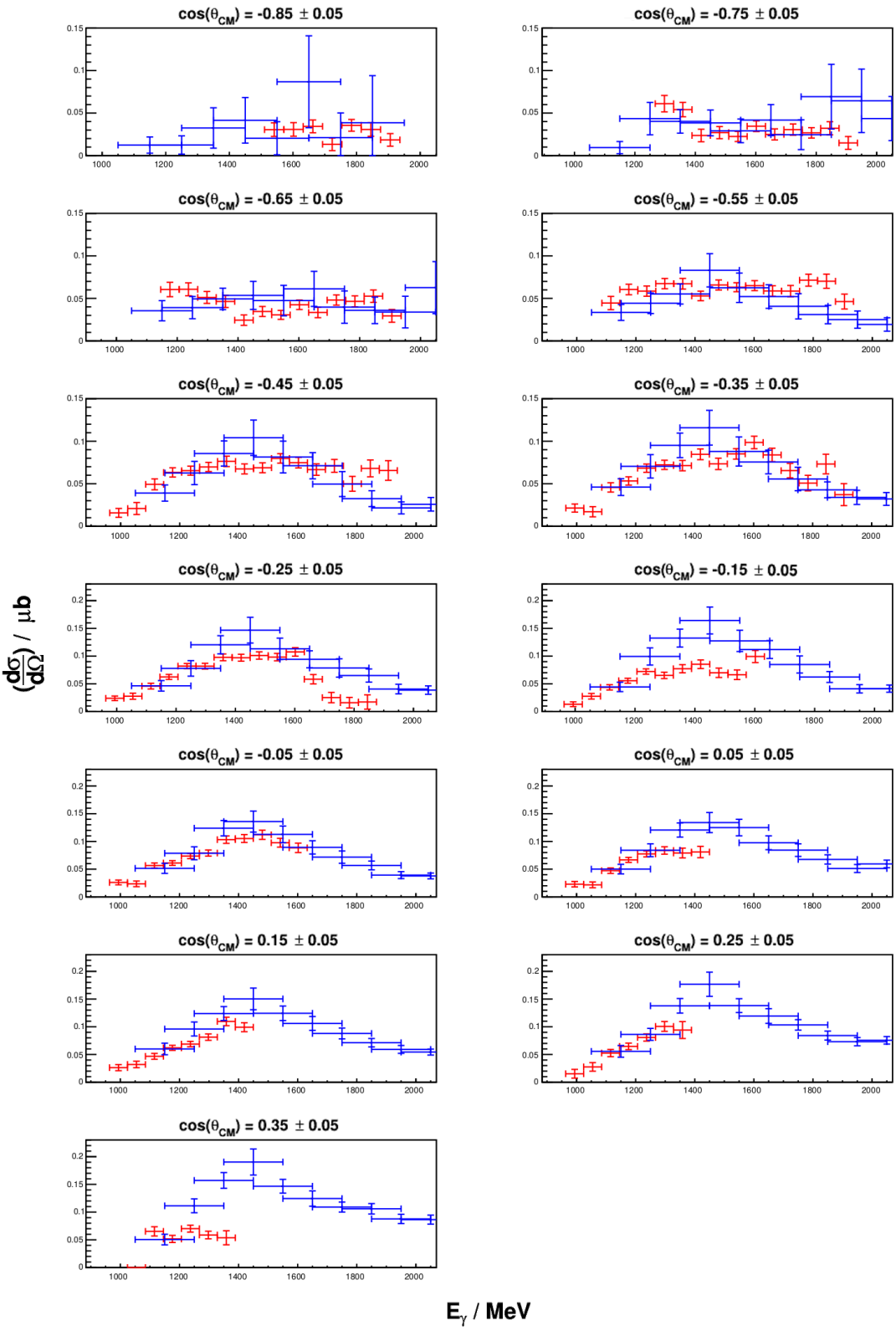

Figure 5.1: Differential cross section ($\frac{d\sigma}{d\Omega}$) depending on beam energy E_γ and angle $\cos(\theta_{\mathrm{CMS}})$ as measured by CLAS (blue) [7] and as a result of this thesis (red). Note the change in scale from $\cos(\theta_{\mathrm{CMS}}) = -0.25 \pm 0.05$ on towards more forward angles

longer matches the shape of the CLAS data.

These deviations might most likely be caused by the fact that the differential cross section in the described energetic and angular regions always lies at the edge of the experiment's acceptance. This can clearly be seen in figure 4.12, which shows the simulated detection efficiency with minimum threshold. At the edge of the acceptance, the simulated detection efficiency might be overestimated and could lead to incorrect values for the differential cross section. An increase of the minimum threshold that has been applied to the simulated detection efficiency would be able to discard the affected data points. However, in order to state this cause with certainty, a more thorough investigation of the simulated detection efficiency would be necessary, which goes beyong the scope of this thesis.

Known systematic uncertainties that have an effect on the differential cross section are listed in table 5.1 [23] and accumulate to 13.94%.

Error source	Error percentage
Punch-through correction	11.1
Photon flux	8.0
Beam energy calibration	2.0
Target length	1.8
Summed in quadrature	13.94

Table 5.1: Known systematic uncertainties that have an effect on the scale of the differential cross section [23]

The most important systematic uncertainty originates from the K^+ identification. Besides this, other systematic error sources might be the specific model of the Fermi momentum within the deuteron and the contribution of the $\Sigma^-(1385)$. A thorough investigation of these systematic error sources has not been carried out, as that would exceed the extent of this thesis.

CHAPTER 6

Summary and Outlook

Pronounced dip structures between $K^*\Lambda$ and $K^*\Sigma$ thresholds in $K_S^0\Sigma^+$ photoproduction off the proton are in good accordance with pentaquark models based on vector meson-baryon interactions that were able to predict the recently discovered LHCb pentaquark states in the hidden charm sector [5, 6]. Thus, the strange sector might be explicable by meson-meson and meson-baryon quark models analogously to the charm sector. More fundamental research in the strange sector is needed to resolve this issue. The goal of this thesis was the measurement of the differential cross section of the reaction $\gamma n \to K^+\Sigma^-$, providing complementary data with greater statistical precision to the existing CLAS data set.

We were able to utilize a novel K^+ identification technique in order to identify K^+ inside the BGO calorimeter that originated from photoproduction off a liquid deuterium and a liquid hydrogen target. The K^+ identification proved to be effective with a maximum simulated detection efficiency of about 6%.

The data sets from the liquid hydrogen and liquid deuterium beam times were normalized with respect to integrated photon flux and target area density as well as corrected for the K^+ punch-through effect. In addition to that, the hydrogen data set was corrected with regard to the Fermi momentum. This enabled us to subtract the data sets and get rid of background channels originating from photoproduction off the proton, reducing the possible decay channels to $K^+\Sigma^-$ and $K^+\Sigma^-(1385)$.

Investigating individual energy and angle bins showed that a direkt Gaussian fit to the missing mass spectra containing the two peaks was impossible, as the spectra appeared to be non-continous, which was caused by the fact that we limited the K^+ identification to incident hits within a single crystal only. To handle this, we attempted to use Roofit to separate $K^+\Sigma^-$ from $K^+\Sigma^-(1385)$. As the contribution from $K^+\Sigma^-(1385)$ appeared to be quite low and error ranges from the data that had to be fitted to were quite large, the contribution of $K^+\Sigma^-(1385)$ was neglected.

For individual energy bins, the missing mass spectra contained negative entries resulting from the subtraction of the Fermi-broadened proton data set. As the Fermi momentum correction mostly affected the shape of the signal, but the integral only to neglectable 1.23%, we were able to take the full integral over the missing mass spectra, even with negative entries within, and still yield valid results.

The obtained integrals were divided by the simulated detection efficiency and the solid angle element, yielding the differential cross section ($\frac{d\sigma}{d\Omega}$) of the reaction $\gamma n \rightarrow K^+\Sigma^-$ dependent on beam energy E_γ and angle $\cos(\theta_{\mathrm{CMS}})$.

Comparing the obtained data to data from CLAS showed good agreement from the angle $\cos(\theta_{\mathrm{CMS}}) = -0.85$ to $\cos(\theta_{\mathrm{CMS}}) = -0.35$. It is worth mentioning that our data utilized a finer energy binning and generally inherited much smaller error ranges. Discrepancies occur from $\cos(\theta_{\mathrm{CMS}}) = -0.25$ and more forward angles at high energies, as the differential cross section declines to an extent that no longer matches the shape of the CLAS data. This might possibly be caused by the fact that these data points lie at the edge of the experiment's acceptance, where the simulated detection efficiency could be too high.

Known systematic errors that have an effect on the differential cross section accumulate to 13.94%. For future analysis, systematic errors resulting from the K^+ identification, the specific Fermi momentum model and the contribution of $K^+\Sigma^-(1385)$ should be analysed. Furthermore, one could extend the covered angular range by making use of the forward spectrometer.

Bibliography

[1] U. Löring, B. C. Metsch and H. R. Petry,
The Light baryon spectrum in a relativistic quark model with instanton induced quark forces: The nonstrange baryon spectrum and ground states, Eur. Phys. J. **A10** (2001) 395,
URL: `https://arxiv.org/abs/hep-ph/0103289` (cit. on pp. 1, 2).

[2] H. Schmieden for the BGO–OD Collaboration,
First Results from the BGO–OD Experiment at ELSA, Few-Body Systems **59** (2018) 135,
URL: `https://doi.org/10.1007/s00601-018-1453-0` (cit. on pp. 1, 5).

[3] R. J. Jaffe, *Multiquark hadrons. I. Phenomenology of $Q^2\overline{Q}^2$ mesons*,
Phys. Rev. D **15** (1977) 267,
URL: `https://link.aps.org/doi/10.1103/PhysRevD.15.267` (cit. on p. 2).

[4] A. Manohar and H. Georgi, *Chiral quarks and the non-relativistic quark model*,
Nuclear Physics B **234** (1984) 189,
URL: `http://www.sciencedirect.com/science/article/pii/0550321384902311`
(cit. on p. 2).

[5] R. Aaij et al. (LHCb Collaboration),
Observation of $J/\psi p$ Resonances Consistent with Pentaquark States in $\Lambda_b^0 \to J/\psi K^- p$ Decays,
Phys. Rev. Lett. **115** (2015) 072001,
URL: `https://link.aps.org/doi/10.1103/PhysRevLett.115.072001`
(cit. on pp. 2, 15, 31).

[6] A. Ramos and E. Oset, *The role of vector-baryon channels and resonances in the $\gamma p \to K^0\Sigma^+$ and $\gamma n \to K^0\Sigma^0$ reactions near the $K^*\Lambda$ threshold*, Physics Letters B **727** (2013) 287,
URL: `http://www.sciencedirect.com/science/article/pii/S0370269313008058`
(cit. on pp. 2, 15, 31).

[7] S.A. Pereira et al., *Differential cross section of γn to $K^+\Sigma^-$ on bound neutrons with incident photons from 1.1 to 3.6 GeV*, Phys. Lett. **B688** (2010) 289,
URL: `https://arxiv.org/abs/0912.4833` (cit. on pp. 2, 27, 28).

[8] Arbeitsgruppe ELSA am Physikalischen Institut der Universität Bonn, *Overview of ELSA*,
URL: `https://www-elsa.physik.uni-bonn.de/Beschleuniger/bilder/ELSA-Plan_en_gross.png` (cit. on p. 6).

[9] Arbeitsgruppe ELSA am Physikalischen Institut der Universität Bonn, *ELSA Home Page*,
URL: `https://www-elsa.physik.uni-bonn.de/index.html` (cit. on p. 5).

[10] G. Scheluchin, *Meson photoproduction on the proton using the BGO-OD detector complemented by a new Scintillating Ring (SciRi)*, MA thesis: Universität Bonn, 2015, URL: https://www.hsag.physik.uni-bonn.de/forschung/diplom-doktorarbeiten/diplom-masterarbeiten/Masterarbeit_GeorgScheluchin.pdf (cit. on pp. 7–9).

[11] A. Bella, *Linearly polarised photon beams at the BGO-OD experiment at ELSA*, PhD thesis: Universität Bonn, 2016, URL: http://hss.ulb.uni-bonn.de/2016/4493/4493.pdf (cit. on pp. 7, 8).

[12] B.-E. Reitz, *Coherent bremsstrahlung with the scintillating fiber detector of the BGO-OD tagging system*, MA thesis: Universität Bonn, 2015, URL: https://www.hsag.physik.uni-bonn.de/forschung/diplom-doktorarbeiten/diplom-masterarbeiten/Masterarbeit_Bjoern-EricReitz.pdf (cit. on p. 8).

[13] S. Alef, *Scintillating fibre detector and kinematicfitting for the BGO-OD experiment*, MA thesis: Universität Bonn, 2015, URL: https://www.hsag.physik.uni-bonn.de/forschung/diplom-doktorarbeiten/diplom-masterarbeiten/Masterarbeit_Stefan%20Alef.pdf (cit. on p. 8).

[14] K. Kohl, *Absolute Photon Flux Measurement at the BGO-OD-Experiment*, MA thesis: Universität Bonn, 2016, URL: https://www.hsag.physik.uni-bonn.de/forschung/diplom-doktorarbeiten/diplom-masterarbeiten/Masterarbeit_KatrinKohl.pdf (cit. on p. 8).

[15] P. Bauer, *Track and vertex reconstruction in the BGO-OD experiment using the central MWPC*, MA thesis: Universität Bonn, 2017, URL: https://www.hsag.physik.uni-bonn.de/forschung/diplom-doktorarbeiten/diplom-masterarbeiten/masterarbeit-patrickbauer.pdf (cit. on p. 9).

[16] F. Messi, *The Tagging System of the BGO-OD experiment*, PhD thesis: Universität Bonn, 2015, URL: http://hss.ulb.uni-bonn.de/2015/4028/4028.pdf (cit. on p. 9).

[17] S. Böse, *Aufbau und Test eines Szintillationsfaser-Detektors für das neue Vorwärtsspektrometer an ELSA*, PhD thesis: Universität Bonn, 2016, URL: http://hss.ulb.uni-bonn.de/2016/4300/4300.pdf (cit. on p. 9).

[18] T. Frese, *In situ field measurement of the Open Dipole magnet at the BGO-OD experiment*, MA thesis: Universität Bonn, 2012, URL: https://www.hsag.physik.uni-bonn.de/forschung/diplom-doktorarbeiten/diplom-masterarbeiten/Diplomarbeit_TorstenFrese.pdf (cit. on p. 9).

[19] T. Schwan, *Test und Inbetriebnahme der Driftkammern für das BGO-OD-Spektrometer*, Universität Bonn, 2010,
URL: https://www.hsag.physik.uni-bonn.de/forschung/diplom-doktorarbeiten/diplom-masterarbeiten/Diplomarbeit_TimoSchwan.pdf
(cit. on p. 9).

[20] P. Meiß, *The Time Of Flight Spectrometer of the BGO-OD Experiment*, Universität Bonn, 2013,
URL: https://www.hsag.physik.uni-bonn.de/forschung/diplom-doktorarbeiten/diplom-masterarbeiten/Diplomarbeit_PeterMeiss.pdf
(cit. on p. 10).

[21] T. Jude et al., *$K^+\Lambda$ and $K^+\Sigma^0$ photoproduction with fine center-of-mass energy resolution*, Physics Letters B **735** (2014) 112,
URL: http://www.sciencedirect.com/science/article/pii/S0370269314004109
(cit. on pp. 11, 13).

[22] M. Tanabashi et al. (Particle Data Group), *Review of Particle Physics*, Phys. Rev. D **98** (2018) 030001,
URL: https://link.aps.org/doi/10.1103/PhysRevD.98.030001 (cit. on p. 11).

[23] T. Jude, *Private communication*, 2019 (cit. on pp. 11, 12, 29).

[24] R. Machleidt, K. Holinde and C. Elster,
The Bonn meson-exchange model for the nucleon—nucleon interaction,
Physics Reports **149** (1987) 1,
URL: http://www.sciencedirect.com/science/article/pii/S0370157387800029
(cit. on p. 17).

[25] National Institue of Standards and Technology, *NIST Chemistry WebBook, SRD 69*,
URL: https://webbook.nist.gov/chemistry/name-ser/ (cit. on p. 21).

[26] S. Agostinelli et al., *Geant4 — a simulation toolkit*,
Nuclear Instruments and Methods in Physics Research Section A: Accelerators, Spectrometers, Detectors and Associated Equipment **506** (2003) 250,
URL: http://www.sciencedirect.com/science/article/pii/S0168900203013688
(cit. on p. 25).

APPENDIX A

Obtained Data

$\cos(\theta_{\mathrm{CMS}})$	$\Delta\cos(\theta_{\mathrm{CMS}})$	E_γ / MeV	ΔE_γ / MeV	$(\frac{d\sigma}{d\Omega})$ / µb	$\Delta(\frac{d\sigma}{d\Omega})$ / µb
-0.85	0.05	1540.97	30.41	0.030488	0.007976
-0.85	0.05	1601.79	30.41	0.030760	0.007996
-0.85	0.05	1662.61	30.41	0.034331	0.007531
-0.85	0.05	1723.43	30.41	0.013246	0.007436
-0.85	0.05	1784.25	30.41	0.035562	0.006907
-0.85	0.05	1845.07	30.41	0.030679	0.008000
-0.85	0.05	1905.89	30.41	0.018437	0.007396
-0.75	0.05	1297.70	30.41	0.061054	0.009673
-0.75	0.05	1358.51	30.41	0.054095	0.008455
-0.75	0.05	1419.33	30.41	0.023623	0.007359
-0.75	0.05	1480.15	30.41	0.026986	0.007123
-0.75	0.05	1540.97	30.41	0.022479	0.005918
-0.75	0.05	1601.79	30.41	0.034525	0.006275
-0.75	0.05	1662.61	30.41	0.024890	0.006508
-0.75	0.05	1723.43	30.41	0.030549	0.006630
-0.75	0.05	1784.25	30.41	0.026712	0.006101
-0.75	0.05	1845.07	30.41	0.032125	0.007695
-0.75	0.05	1905.89	30.41	0.014858	0.007550
-0.65	0.05	1176.06	30.41	0.060453	0.008466
-0.65	0.05	1236.88	30.41	0.060688	0.007600
-0.65	0.05	1297.70	30.41	0.051109	0.007025
-0.65	0.05	1358.51	30.41	0.046389	0.007141
-0.65	0.05	1419.33	30.41	0.024402	0.006116
-0.65	0.05	1480.15	30.41	0.034614	0.005895
-0.65	0.05	1540.97	30.41	0.030580	0.005274
-0.65	0.05	1601.79	30.41	0.042511	0.005585
-0.65	0.05	1662.61	30.41	0.033413	0.006107

-0.65	0.05	1723.43	30.41	0.048074	0.006033
-0.65	0.05	1784.25	30.41	0.046504	0.006474
-0.65	0.05	1845.07	30.41	0.052617	0.007302
-0.65	0.05	1905.89	30.41	0.029432	0.007507
-0.55	0.05	1115.24	30.41	0.044532	0.007804
-0.55	0.05	1176.06	30.41	0.060483	0.006172
-0.55	0.05	1236.88	30.41	0.058553	0.006006
-0.55	0.05	1297.70	30.41	0.067393	0.006037
-0.55	0.05	1358.51	30.41	0.067219	0.006277
-0.55	0.05	1419.33	30.41	0.052881	0.005628
-0.55	0.05	1480.15	30.41	0.065760	0.005898
-0.55	0.05	1540.97	30.41	0.063132	0.005296
-0.55	0.05	1601.79	30.41	0.065031	0.005874
-0.55	0.05	1662.61	30.41	0.058723	0.006188
-0.55	0.05	1723.43	30.41	0.058594	0.006629
-0.55	0.05	1784.25	30.41	0.071414	0.007055
-0.55	0.05	1845.07	30.41	0.070203	0.008322
-0.55	0.05	1905.89	30.41	0.046281	0.008736
-0.45	0.05	993.60	30.41	0.015690	0.005215
-0.45	0.05	1054.42	30.41	0.020827	0.007058
-0.45	0.05	1115.24	30.41	0.049263	0.00643
-0.45	0.05	1176.06	30.41	0.063308	0.005449
-0.45	0.05	1236.88	30.41	0.065354	0.005308
-0.45	0.05	1297.70	30.41	0.069734	0.005369
-0.45	0.05	1358.51	30.41	0.076297	0.006127
-0.45	0.05	1419.33	30.41	0.067413	0.005874
-0.45	0.05	1480.15	30.41	0.068765	0.005847
-0.45	0.05	1540.97	30.41	0.079786	0.005579
-0.45	0.05	1601.79	30.41	0.074765	0.006219
-0.45	0.05	1662.61	30.41	0.066625	0.006735
-0.45	0.05	1723.43	30.41	0.070994	0.007559
-0.45	0.05	1784.25	30.41	0.049905	0.008733
-0.45	0.05	1845.07	30.41	0.068008	0.009925
-0.45	0.05	1905.89	30.41	0.065555	0.011546
-0.35	0.05	993.60	30.41	0.021367	0.004773
-0.35	0.05	1054.42	30.41	0.017022	0.005985
-0.35	0.05	1115.24	30.41	0.045661	0.005491
-0.35	0.05	1176.06	30.41	0.053240	0.004868
-0.35	0.05	1236.88	30.41	0.068269	0.004872
-0.35	0.05	1297.70	30.41	0.072217	0.005418

-0.35	0.05	1358.51	30.41	0.071302	0.006110
-0.35	0.05	1419.33	30.41	0.084590	0.006292
-0.35	0.05	1480.15	30.41	0.073360	0.006687
-0.35	0.05	1540.97	30.41	0.085083	0.006176
-0.35	0.05	1601.79	30.41	0.098542	0.007336
-0.35	0.05	1662.61	30.41	0.083883	0.007888
-0.35	0.05	1723.43	30.41	0.065413	0.008490
-0.35	0.05	1784.25	30.41	0.050735	0.009141
-0.35	0.05	1845.07	30.41	0.073151	0.011532
-0.35	0.05	1905.89	30.41	0.037167	0.012950
-0.25	0.05	993.60	30.41	0.023903	0.004108
-0.25	0.05	1054.42	30.41	0.027659	0.005485
-0.25	0.05	1115.24	30.41	0.045863	0.005198
-0.25	0.05	1176.06	30.41	0.062451	0.004518
-0.25	0.05	1236.88	30.41	0.082012	0.004677
-0.25	0.05	1297.70	30.41	0.081846	0.005176
-0.25	0.05	1358.51	30.41	0.097767	0.006077
-0.25	0.05	1419.33	30.41	0.097108	0.006237
-0.25	0.05	1480.15	30.41	0.101079	0.006627
-0.25	0.05	1540.97	30.41	0.098217	0.006670
-0.25	0.05	1601.79	30.41	0.107564	0.007651
-0.25	0.05	1662.61	30.41	0.058319	0.008457
-0.25	0.05	1723.43	30.41	0.025221	0.009300
-0.25	0.05	1784.25	30.41	0.015952	0.009555
-0.25	0.05	1845.07	30.41	0.017208	0.012908
-0.15	0.05	993.60	30.41	0.013197	0.004233
-0.15	0.05	1054.42	30.41	0.027582	0.005045
-0.15	0.05	1115.24	30.41	0.043658	0.004771
-0.15	0.05	1176.06	30.41	0.055611	0.004430
-0.15	0.05	1236.88	30.41	0.072216	0.004823
-0.15	0.05	1297.70	30.41	0.065225	0.005699
-0.15	0.05	1358.51	30.41	0.077251	0.007369
-0.15	0.05	1419.33	30.41	0.085327	0.007742
-0.15	0.05	1480.15	30.41	0.069887	0.008470
-0.15	0.05	1540.97	30.41	0.066380	0.008648
-0.15	0.05	1601.79	30.41	0.099311	0.010944
-0.05	0.05	993.60	30.41	0.026035	0.004322
-0.05	0.05	1054.42	30.41	0.023496	0.005087
-0.05	0.05	1115.24	30.41	0.056516	0.004647
-0.05	0.05	1176.06	30.41	0.061089	0.004237

-0.05	0.05	1236.88	30.41	0.073610	0.004675
-0.05	0.05	1297.70	30.41	0.079057	0.005522
-0.05	0.05	1358.51	30.41	0.103243	0.006699
-0.05	0.05	1419.33	30.41	0.105260	0.007115
-0.05	0.05	1480.15	30.41	0.112012	0.008304
-0.05	0.05	1540.97	30.41	0.097644	0.007957
-0.05	0.05	1601.79	30.41	0.088444	0.008484
0.05	0.05	993.60	30.41	0.022890	0.004891
0.05	0.05	1054.42	30.41	0.021682	0.005221
0.05	0.05	1115.24	30.41	0.047248	0.004936
0.05	0.05	1176.06	30.41	0.066675	0.004508
0.05	0.05	1236.88	30.41	0.077477	0.005359
0.05	0.05	1297.70	30.41	0.083733	0.006695
0.05	0.05	1358.51	30.41	0.079146	0.008804
0.05	0.05	1419.33	30.41	0.080950	0.010232
0.15	0.05	993.60	30.41	0.026288	0.005502
0.15	0.05	1054.42	30.41	0.032001	0.005829
0.15	0.05	1115.24	30.41	0.046683	0.005281
0.15	0.05	1176.06	30.41	0.062000	0.004525
0.15	0.05	1236.88	30.41	0.068746	0.004925
0.15	0.05	1297.70	30.41	0.081287	0.005810
0.15	0.05	1358.51	30.41	0.109600	0.007645
0.15	0.05	1419.33	30.41	0.099195	0.008074
0.25	0.05	993.60	30.41	0.015254	0.007909
0.25	0.05	1054.42	30.41	0.027620	0.007743
0.25	0.05	1115.24	30.41	0.052551	0.006509
0.25	0.05	1176.06	30.41	0.064616	0.005901
0.25	0.05	1236.88	30.41	0.080655	0.006490
0.25	0.05	1297.70	30.41	0.100604	0.008854
0.25	0.05	1358.51	30.41	0.094083	0.015223
0.35	0.05	1054.42	30.41	0.000000	0.000000
0.35	0.05	1115.24	30.41	0.065222	0.008342
0.35	0.05	1176.06	30.41	0.051587	0.006417
0.35	0.05	1236.88	30.41	0.070141	0.006262
0.35	0.05	1297.70	30.41	0.058644	0.006840
0.35	0.05	1358.51	30.41	0.053674	0.012656

APPENDIX B

Derivation of Formula for $E_{K^+}^{\text{kin}}$

Formula 4.5 describes the true kinetic energy of a K^+ depending on initial energy, momentum and K^+ angle in the laboratory frame θ_{LAB}. It is used to get rid of flawed data points caused by K^+ that penetrated the BGO crystals deep enough so that they decayed right in front of the photomultiplier tubes, causing issues with the readout of the signal. It shall be derived here, starting from four momentum conservation:

$$p_\gamma + p_{\text{target}} = p_{K^+} + p_{\Sigma^-} \tag{B.1}$$

Define $p_{\text{initial}} = p_\gamma + p_{\text{target}}$*:*

$$\begin{aligned}
p_{\text{initial}} &= p_{K^+} + p_{\Sigma^-} && \text{(B.2)}\\
p_{\Sigma^-}^2 &= (p_{\text{initial}} - p_{K^+})^2 && \text{(B.3)}\\
&= p_{\text{initial}}^2 + m_{K^+}^2 - 2p_{\text{initial}}p_{K^+} && \text{(B.4)}\\
&= p_{\text{initial}}^2 + m_{K^+}^2 - 2E_{\text{initial}}E_{K^+} + 2|\vec{p}_{\text{initial}}||\vec{p}_{K^+}|\cos(\theta_{\text{LAB}}) && \text{(B.5)}
\end{aligned}$$

With $p_{\Sigma^-}^2 = E_{\Sigma^-}^2 - \vec{p}_{\Sigma^-}^2 = m_{\Sigma^-}^2$*:*

$$(m_{\Sigma^-}^2 - p_{\text{initial}}^2 - m_{K^+}^2 + 2E_{\text{initial}}E_{K^+})^2 = (2|\vec{p}_{\text{initial}}||\vec{p}_{K^+}|\cos(\theta_{\text{LAB}}))^2 \tag{B.6}$$

Define $A = -m_{\Sigma^-}^2 + p_{\text{initial}}^2 + m_{K^+}^2$*:*

$$\begin{aligned}
(-A + 2E_{\text{initial}}E_{K^+})^2 &= (2|\vec{p}_{\text{initial}}||\vec{p}_{K^+}|\cos(\theta_{\text{LAB}}))^2 && \text{(B.7)}\\
A^2 - 4AE_{\text{initial}}E_{K^+} + 4E_{\text{initial}}^2E_{K^+}^2 &= 4|\vec{p}_{\text{initial}}|^2(E_{K^+}^2 - m_{K^+}^2)\cos^2(\theta_{\text{LAB}}) && \text{(B.8)}\\
0 &= E_{K^+}^2 + E_{K^+}\frac{-4AE_{\text{initial}}}{4E_{\text{initial}}^2 - 4|\vec{p}_{\text{initial}}|^2\cos^2(\theta_{\text{LAB}})}\\
&\quad + \frac{A^2 + 4|\vec{p}_{\text{initial}}|^2 m_{K^+}^2\cos^2(\theta_{\text{LAB}})}{4E_{\text{initial}}^2 - 4|\vec{p}_{\text{initial}}|^2\cos^2(\theta_{\text{LAB}})} && \text{(B.9)}
\end{aligned}$$

Applying p-q formula yields:

$$E_{K^+1/2} = \frac{4AE_{\text{initial}}}{2(4E_{\text{initial}}^2 - 4|\vec{p}_{\text{initial}}|^2\cos^2(\theta_{\text{LAB}}))} \pm \sqrt{\left(\frac{-4AE_{\text{initial}}}{2(4E_{\text{initial}}^2 - 4|\vec{p}_{\text{initial}}|^2\cos^2(\theta_{\text{LAB}}))}\right)^2 - \frac{A^2 + 4|\vec{p}_{\text{initial}}|^2 m_{K^+}^2\cos^2(\theta_{\text{LAB}})}{4E_{\text{initial}}^2 - 4|\vec{p}_{\text{initial}}|^2\cos^2(\theta_{\text{LAB}})}} \tag{B.10}$$

$$= \frac{AE_{\text{initial}} \pm \sqrt{A^2E_{\text{initial}}^2 - 4(E_{\text{initial}}^2 - |\vec{p}_{\text{initial}}|^2\cos^2(\theta_{\text{LAB}}))(\frac{A^2}{4} + |\vec{p}_{\text{initial}}|^2 m_{K^+}^2\cos^2(\theta_{\text{LAB}}))}}{2(E_{\text{initial}}^2 - |\vec{p}_{\text{initial}}|^2\cos^2(\theta_{\text{LAB}}))} \tag{B.11}$$

$$= \frac{AE_{\text{initial}} \pm |\vec{p}_{\text{initial}}|\cos(\theta_{\text{LAB}})\sqrt{A^2 - 4m_{K^+}^2(E_{\text{initial}}^2 - |\vec{p}_{\text{initial}}|^2\cos(\theta_{\text{LAB}})^2)}}{2(E_{\text{initial}}^2 - |\vec{p}_{\text{initial}}|)} \tag{B.12}$$

This yields for the kinetic energy:

$$E_{K^+1/2}^{\text{kin}} = \frac{AE_{\text{initial}} \pm |\vec{p}_{\text{initial}}|\cos(\theta_{\text{LAB}})\sqrt{A^2 - 4m_{K^+}^2(E_{\text{initial}}^2 - |\vec{p}_{\text{initial}}|^2\cos(\theta_{\text{LAB}})^2)}}{2(E_{\text{initial}}^2 - |\vec{p}_{\text{initial}}|)} - m_{K^+} \tag{4.5}$$

List of Figures

List of Tables